

**Development of a Tuneable Laser Source in the
Vacuum Ultraviolet and its Applications to
Spectroscopy**

Gareth David Dickenson

Thesis presented in partial fulfillment of the requirements for the degree of



Master of Science at Stellenbosch University

Promotors: Dr. C.M. Steenkamp, Stellenbosch University

and

Prof E.G. Rohwer, Stellenbosch University

December 2008

Declaration

By submitting this thesis electronically, I declare that the entirety of the work contained therein is my own, original work, that I am the owner of the copyright thereof (unless to the extent explicitly otherwise stated) and that I have not previously in its entirety or in part submitted it for obtaining any qualification.

Date: December 2008

Copyright © 2008 Stellenbosch University

All rights reserved

Abstract

Third harmonic generation (THG) in a metal vapour is a nonlinear optical interaction that facilitates the generation of light in the vacuum ultraviolet (VUV) portion of the electromagnetic spectrum. The requirement of the metal vapour medium is that it has a suitably large third order nonlinear susceptibility. The third order susceptibility is further enhanced by a two photon resonance. Zinc and magnesium vapours are such nonlinear media. The THG process can be phase matched by mixing the metal vapour with a noble gas in a specific pressure ratio. The metal vapour noble gas mixture needs to be homogeneous and its temperature needs to be constant to within less than a degree Celsius over a path length of 7 cm. These requirements are satisfied by a crossed heat pipe oven. The heat pipe oven makes use of a dynamic liquid-vapour phase equilibrium in sodium in order to maintain a constant temperature of around 800 degrees Celsius, thus facilitating the generation of a stable homogeneous medium of metal vapour and noble gas that can be used for efficient generation of VUV radiation. The development of such a VUV source using zinc vapour and the application of a similar VUV source using magnesium vapour are discussed. The VUV radiation has been applied to laser induced fluorescence spectroscopy of carbon monoxide ($^{12}\text{C}^{16}\text{O}$ and $^{13}\text{C}^{16}\text{O}$). Spectral lines of 20 spin-forbidden singlet-triplet transitions of the $e^3\Sigma^- - X^1\Sigma^+(5\ 0)$ band were detected and accurate experimental wavelengths determined for the first time for five of these lines.

Samevatting

Derde harmoniek opwekking (DHO) in 'n metaaldamp is 'n nie-lineêre interaksie wat lig in the vakuum ultraviolet (VUV) gebied van die elektromagnetiese spektrum kan genereer. 'n Groot derde order nie-lineêre suseptibiliteit is een van die makroskopiese vereistes van die metaaldamp. Die derde order nie-lineêre suseptibiliteit word ook vegroot deur 'n twee-foton resonans. Sink en magnesium is twee tipe nie-lineêre media. Die bydraes tot die derde harmoniek veld wat in verskillende volume-elemente van die medium opgewek is moet konstruktief interfereer: dit word bereik deur die byvoeging van 'n edelgas met 'n bepaalde druk verhouding tussen die metaaldamp en edelgas. Die metaaldamp edelgas mengsel moet homogeen wees en die temperatuur moet konstant gehou word met minder as een graad Celsius verskil oor 'n padlengte van ongeveer 7 cm. Daar word aan hierdie vereistes voldoen deur gebruik te maak van 'n kruisvormige hittepyl-oond. Die hittepyl-oond maak gebruik van 'n dinamiese vloeistof-damp fase ewewig in natrium, om die temperatuur konstant te hou by 800 grade Celsius en sodoende die skepping van 'n stabiele homogene medium van metaaldamp en edelgas geskik vir DHO moontlik te maak. Die ontwikkeling van so 'n tipe VUV bron met sinkdamp en die aanwending van 'n VUV bron wat magnesium as nie-lineêr medium gebruik is bespreek. Die VUV straling is gebruik vir laser geïnduseerde fluoresensie spektroskopie van koolstof monoksied ($^{12}\text{C}^{16}\text{O}$ en $^{13}\text{C}^{16}\text{O}$) te meet. Spektraal lyne van twintig spin-verbode singlet-triplet oorgange van die $e^3\Sigma^- - X^1\Sigma^+(5\ 0)$ band is waargeneem en akurate eksperimentele golflengtes is vir die eerste keer bepaal vir vyf van die lyne.

Acknowledgments

First and foremost I must acknowledge my two supervisors, Dr C.M. Steenkamp and Prof E.G. Rohwer, for their support over the past two years. Your expertise in this field has proved invaluable. The guidance provided as well as the many helpful discussions are most appreciated.

Mr U.G.K. Deutschlander, Mr E Shields and Mr J Germishuizen provided the technical support without which this project would not have taken place. It is with much gratitude that I thank them for their support and patience over the last two years.

A big thank you to Mr J Burns and Mr B Botha whose wizardry in the workshop left me in awe at times! Many of the parts used in the construction of this experiment were made by them.

To all my fellow students and personnel at the Physics Department of the University of Stellenbosch, it has been a wild ride and one that I have enjoyed immensely! Thank you for all the great memories.

To all my friends at the Maties Hockey club thank you so much for giving me something to take my mind off my lasers!

And finally to my mother, father and sister. I appreciate all the love, support and belief you have given me! Even when you had no idea what I was talking about or doing in my laboratory you continued to support me and listen to what I had to say! I cannot thank you enough!

List of Figures

2.1	Resonances	23
2.2	Second Harmonic Generation	27
2.3	The solutions to the coupled differential equations for second harmonic generation.	29
2.4	Third Harmonic Generation	30
2.5	Phase matching curve for three different optical depths	33
2.6	Refractive index of a uniaxial crystal	37
2.7	Energy Level Diagram of Zn	39
2.8	Principle of a Heat Pipe	43
2.9	Heat Pipe Oven developed by Vidal <i>et al</i>	44
2.10	Crossed Heat Pipe Oven	45
2.11	Rovibronic structure of a diatomic molecule.	47
2.12	Potential energy curves of CO	49
3.1	Setup for THG in a zinc heat pipe oven	51
3.2	The frequency doubling unit	55
3.3	Setup for VUV spectroscopy of CO	59
4.1	An optogalvanic spectrum of Neon	63
4.2	Calibration curve for the optogalvanic spectrum	64
4.3	A tuning curve	65
4.4	Power broadening	66
4.5	Malus's law	67
4.6	Percent polarization of the dye laser	68
4.7	Percent transmission of the dye laser through the GTLP	69
4.8	Pulse shape of the dye laser	70
4.9	Phase matching curve of the BBO crystal	71
4.10	Phase matching not adjusted as wavelength is tuned for the BBO crystal	72
4.11	Phase matching curve of the Mg heat pipe oven.	73
4.12	Two photon resonance of magnesium	73
4.13	Two photon resonance of zinc	74
4.14	Singlet spectrum of $^{12}\text{C}^{16}\text{O}$	77
4.15	Singlet spectrum of $^{13}\text{C}^{16}\text{O}$	78

4.16	The calibration curve for the measurements of the singlet spectra of $^{12}\text{C}^{16}\text{O}$ and $^{13}\text{C}^{16}\text{O}$	78
4.17	Rotational Constants of $^{12}\text{C}^{16}\text{O}$	79
4.18	A comparison between the delay scans for a singlet-singlet transition and a singlet-triplet transition.	80
4.19	Triplet spectra	81
4.21	Unresolved triplet lines	81
4.20	Resolved triplet lines	82
4.22	Deviation of measured triplet lines from literature values	84
4.23	Average triplet measurement minus literature wavelengths	85
4.24	The measured values minus the average shift from the calculated literature values.	85
4.25	Unresolved triplet lines and their deviation from the calculated values in the literature	86

Contents

1	Introduction and Outline	10
1.1	Introduction and Motivation	10
1.2	Objectives of Thesis.	11
1.3	Outline of Thesis.	12
2	Theoretical Background	13
2.1	Nonlinear Polarization	13
2.2	Light Propagation in a Nonlinear Material	16
2.2.1	Coupled Waves in a Nonlinear Medium	16
2.2.2	The Slowly Varying Amplitude Approximation	17
2.3	Nonlinear Susceptibility	18
2.3.1	Derivation of the Nonlinear Susceptibilities using the Schrödinger Formalism.	18
2.3.2	Resonant Enhancement	22
2.3.3	Symmetry Properties of the Nonlinear Susceptibilities	24
2.3.3.1	Intrinsic Permutation Symmetry	24
2.3.3.2	Lossless Media	25
2.3.3.3	Spatial Symmetries	25
2.4	The Coupled Wave Equations	26
2.4.1	The Coupled Wave Equations for Second Harmonic Generation	26
2.4.2	The Coupled Wave Equations for Third Harmonic Generation	29
2.4.3	The Coupled Wave Equations for Four Photon Sum Frequency Generation	31
2.5	Phase Matching	34
2.5.1	Properties of the BBO Crystal	34
2.5.2	Phase Matching in a BBO Crystal	35
2.5.3	Phase Matching in a Gaseous Medium	38
2.6	Zinc and Magnesium Vapour as Nonlinear Media	39
2.7	The Heat Pipe and its Application to Spectroscopy	41
2.7.1	Brief History of the Heat Pipe	41
2.7.2	Description of the Heat Pipe.	42
2.7.3	Properties of the Heat Pipe Oven	43

2.7.4	The Crossed Heat Pipe Oven	44
2.8	VUV Spectroscopy of Carbon Monoxide	46
2.8.1	Introduction to CO	46
2.8.2	Rovibronic Spectra	46
3	Experimental Method	51
3.1	Setup for Four Wave Mixing in Zn Vapour	51
3.1.1	Lasers Optimisation and Calibration	52
3.1.2	Second Harmonic Generation in a BBO Crystal	54
3.1.3	Construction and Development of the Heat Pipe Oven	55
3.1.4	Four Wave Mixing in Zinc Vapour	58
3.1.4.1	Setup for Resonant Enhancement using the $5s^1S_0$ Level	58
3.1.4.2	Setup for Resonant Enhancement using the $4s6s^1S$ Level	58
3.2	Setup for VUV Spectroscopy of CO	59
3.2.1	Setup for Sum Frequency Generation in a Magnesium Vapour	59
3.2.2	LIF Spectroscopy of CO	60
3.2.2.1	Detection of Singlet-Singlet Transitions	61
3.2.2.2	Detection of Singlet-Triplet Transitions	61
4	Experimental Results and Discussion	62
4.1	Dye Laser Characterisation	62
4.1.1	Dye Laser Calibration	62
4.1.2	Limitations of the Calibration Technique	62
4.1.3	Polarization of the Dye Laser	64
4.1.4	Pulse Shape of the Dye Laser	65
4.2	Characterisation of the Frequency Doubling Unit	66
4.2.1	Experiments with Rhodamine B Dye	67
4.2.1.1	Phase Matching	67
4.2.1.2	Experiments with Lenses	68
4.2.1.3	The Dependence of the Phase Matching Angle on the Wavelength	69
4.3	Experimental Results for Four Wave Mixing in a Metal Vapour	70
4.3.1	Experimental Results for Sum Frequency Generation in Mg Vapour	70
4.3.2	Experimental Results for Third Harmonic Generation and Sum Frequency Generation in Zn Vapour	71
4.3.2.1	Resonant Enhancement using the $5s^1S_0$ Level	71
4.3.2.2	Resonant Enhancement using the $4s6s^1S$ Level	75
4.4	Spectroscopy of CO with an Existing VUV source	76
4.4.1	Calibration and Results on Rotational Constants	76
4.4.2	Optimisation of the Setup for the Detection of Forbidden Transitions	76
4.4.3	Results on Forbidden Transitions	80

<i>CONTENTS</i>	9
5 Conclusion	87
5.1 Generation of VUV by Four-Wave-Mixing in Metal Vapours . . .	87
5.2 VUV Spectroscopy of CO	88
5.3 Proposed Future Work	88

Chapter 1

Introduction and Outline

1.1 Introduction and Motivation

The advent of the laser is described by many as one of the greatest inventions in the history of science [1]. It has led to many spheres of physics being developed; one of them is the field of nonlinear optics.

Shortly after the first working laser in 1960 Franken *et al* [2] observed the phenomenon of second harmonic generation in 1961. This was the beginning of the field of nonlinear optics. The theoretical side of optical wave mixing was pioneered by Armstrong *et al* [3] in 1962.

Today nonlinear interactions have a wide range of commercial and industrial applications. In the area of experimental science one of the most useful applications lies in generating radiation in regions of the electromagnetic spectrum that was previously unreachable with the available laser source. This ability to effectively tune a laser over a specific wavelength region coupled with the fact that lasers have extremely narrow bandwidth make them the perfect tool for high resolution spectroscopy. Sum and difference frequency crystals provide extended tuneability in the visible and infrared region. These crystals become opaque around 200 nm and cannot be used to generate wavelengths below this point. Many atoms and molecules such as CO and NO exhibit spectroscopic features in the wavelength region below 200 nm yet there are currently no commercially available laser sources producing tuneable, narrow bandwidth radiation in this wavelength range. However, nonlinear interactions in transparent gaseous media provide us with an indirect method of accessing this region in the electromagnetic spectrum. Four wave sum mixing in a gaseous nonlinear medium is one such method and forms the focus of the present study. In general four

wave sum mixing is the interaction of four electromagnetic waves in a nonlinear medium. In the work presented here, we make use of third harmonic generation and sum frequency generation in zinc and magnesium vapour to generate coherent radiation in the vacuum ultraviolet (VUV) region of the spectrum. For third harmonic generation a beam at frequency ω_1 interacts in the metal vapour medium generating radiation at frequency $3\omega_1$. The setup can then be modified by adding another beam at frequency ω_2 to produce tuneable sum frequency radiation at frequency $\omega_{sf} = \omega_1 + \omega_1 + \omega_2$. The wavelength region that one can access with the sum frequency radiation ω_{sf} is dependent on the choice of nonlinear material. The three main metal vapours used for four wave mixing are magnesium, zinc and mercury. Magnesium is most efficient for generating tuneable radiation in the wavelength range of 175 - 135 nm, zinc vapour from 140 - 120 nm and mercury from 120 - 104.5 nm [4]. There is currently a functioning magnesium heat pipe that has been employed to measure rovibronic energy levels of carbon monoxide here at Stellenbosch University. The spectroscopic data on carbon monoxide finds its application in astrophysics where the measurements can be used to calculate densities and heliocentric velocities of interstellar molecular clouds [5]. It is hoped that in the future with the new zinc heat pipe it will be possible to continue these measurements at even shorter VUV wavelengths. It is however not only limited to carbon monoxide but there is potential to investigate nitrogen monoxide and it may also be used to determine spectroscopic constants and potential energy curves of excited states of Xe₂, Kr₂ and Ar₂ as reported by Herman *et al* [4]. Another possible use is for the investigation of defect generation in large bandgap materials such as diamond and LiF.

1.2 Objectives of Thesis.

This thesis reports on the generation of vacuum ultraviolet radiation by the four wave mixing process of third harmonic generation and sum frequency generation in a two component gaseous medium consisting of zinc vapour and helium gas. The aim is to completely characterise this system and to optimise all the parameters in the setup so as to increase the efficiency of the process. The zinc vapour helium gas mixture is prepared inside a crossed heat pipe oven. A thorough theoretical study of the four wave mixing process has been undertaken so as to act as a guide when deciding what parameters to optimise in order to achieve

maximum efficiency. A thorough study of the physical principles of a heat pipe oven is conducted so as to achieve the aim of the practical goal: to construct a crossed heat pipe oven for the generation of zinc vapour helium gas mixture. A comparison between zinc vapour and magnesium vapour as nonlinear media is another objective. Finally VUV radiation generated by sum frequency generation in a crossed heat pipe employing magnesium as working material is applied to laser induced fluorescence (LIF) spectroscopy of CO.

1.3 Outline of Thesis.

Chapter 2 presents the necessary theoretical underpinnings of the thesis. It begins with an introduction to nonlinear interactions, how and why they occur. Section 2.2 gives a brief, general description of wave propagation in nonlinear media, such topics as the coupled wave equations and the slowly varying amplitude approximation are covered. In section 2.3 the theory behind nonlinear susceptibilities is presented and the second and third order nonlinear susceptibilities are derived using the Schrödinger formalism. Section 2.4 focuses on the coupled wave equations for second and third harmonic generation. Section 2.5 covers phase matching. Section 2.6 is devoted to the suitability of zinc and magnesium vapour as a nonlinear medium and section 2.7 focusses on the heat pipe oven. Finally section 2.8 reports on an application of the tuneable VUV source, namely VUV spectroscopy of CO.

Chapter 3 is concerned with the experimental apparatus. Section 3.1 provides a detailed description of the experimental setup for four wave sum mixing in a Zn vapour medium and section 3.2 is devoted to the setup for VUV spectroscopy of CO.

In Chapter 4 the measurements are presented and discussed. Section 4.1 is concerned with the dye lasers and the calibration thereof. Section 4.2 reports on the characterisation of the frequency doubling unit. The experimental results for third harmonic generation are given in section 4.3 and the results for sum frequency generation are covered in section 4.4. Spectroscopic results obtained on forbidden transitions of CO at Stellenbosch are discussed in section 4.5.

Conclusions are drawn in chapter 5 and future work is proposed.

Chapter 2

Theoretical Background

2.1 Nonlinear Polarization

Maxwell's equations are the starting point in understanding nonlinear optics. When intense laser light is shone into the metal vapour, it interacts in a nonlinear way and the interaction modifies the optical field. It can be shown through Maxwell's equations that the nonlinear polarization is that quantity that describes the response of the medium to the incident electric field, and is the source of secondary radiation generated in the medium. Maxwell's equations in general are given below (in c.g.s units).

$$\nabla \times \mathbf{E} = -\frac{1}{c} \frac{\partial \mathbf{B}}{\partial t} \quad (2.1)$$

$$\nabla \times \mathbf{H} = \frac{1}{c} \frac{\partial \mathbf{D}}{\partial t} + \frac{4\pi}{c} \mathbf{J} \quad (2.2)$$

$$\nabla \cdot \mathbf{D} = 4\pi\rho \quad (2.3)$$

$$\nabla \cdot \mathbf{B} = 0 \quad (2.4)$$

with $\mathbf{D} = \mathbf{E} + 4\pi\mathbf{P}$ the electric displacement, $\mathbf{B} = \mathbf{H} + 4\pi\mathbf{M}$ the magnetic induction, \mathbf{J} the current density and ρ the charge density. The nonlinear wave equation is derived from equation 2.1 and 2.2. Assumptions are made with regard to the charge and free currents; solutions are found in areas where these quantities are zero and we assume that the material is nonmagnetic so that $\mathbf{B} = \mathbf{H}$. The curl of equation 2.1 is taken and equation 2.2 is inserted into the

resulting formula, to yield

$$\nabla^2 \mathbf{E} - \frac{n^2}{c^2} \frac{d^2 \mathbf{E}}{dt^2} = \frac{4\pi}{c^2} \frac{d^2 \mathbf{P}^{\text{NL}}}{dt^2} \quad (2.5)$$

often called the fundamental equation of nonlinear optics. For the full derivation see [6] or [1]. It is a second order differential equation containing the local electric field \mathbf{E} and the generalised electric polarization \mathbf{P} . \mathbf{P} is a result of polarization from the magnetic dipole, electric dipole and higher order multipoles. In many cases the magnetic dipole and higher order multipoles can be neglected [1]. This is known as the electric dipole approximation. \mathbf{P} then reduces to the electric dipole polarization only. Whenever the right hand side of equation 2.5 is nonzero the nonlinear polarization drives the electric field at frequencies other than the incident electric field. Charges are being accelerated and this generates electromagnetic radiation. It is not always possible to find \mathbf{P} exactly, therefore approximations have to be made. Expand \mathbf{P} into a power series of \mathbf{E} .

$$\begin{aligned} \mathbf{P}(\mathbf{r}, t) = & \int_{-\infty}^{+\infty} \chi^{(1)}(\mathbf{r} - \mathbf{r}', t - t') \cdot \mathbf{E}(\mathbf{r}, t') d\mathbf{r}' dt' + \\ & \int_{-\infty}^{+\infty} \chi^{(2)}(\mathbf{r} - \mathbf{r}_1, t - t_1, \mathbf{r} - \mathbf{r}_2, t - t_2) \cdot \mathbf{E}(\mathbf{r}_1, t_1) \times \mathbf{E}(\mathbf{r}_2, t_2) d\mathbf{r}_1 dt_1 d\mathbf{r}_2 dt_2 + \\ & \int_{-\infty}^{+\infty} \chi^{(3)}(\vec{r} - \mathbf{r}_1, t - t_1, \vec{r} - \mathbf{r}_2, t - t_2, \vec{r} - \mathbf{r}_3, t - t_3) \cdot \mathbf{E}(\mathbf{r}_1, t_1) \times \mathbf{E}(\mathbf{r}_2, t_2) \times \\ & \mathbf{E}(\vec{r}_3, t_3) d\mathbf{r}_1 dt_1 d\mathbf{r}_2 dt_2 d\mathbf{r}_3 dt_3 + \dots \end{aligned} \quad (2.6)$$

The first approximation is to assume that \mathbf{E} is the sum of monochromatic plane waves

$$\mathbf{E}(\mathbf{r}, t) = \sum_b \mathbf{E}(\mathbf{k}_b, \omega_b) \quad (2.7)$$

If 2.7 is inserted into 2.6 then the Fourier transform of 2.6 yields

$$\mathbf{P}(\mathbf{k}, \omega) = \mathbf{P}^{(1)}(\mathbf{k}, \omega) + \mathbf{P}^{(2)}(\mathbf{k}, \omega) + \mathbf{P}^{(3)}(\mathbf{k}, \omega) + \dots \quad (2.8)$$

where

$$\mathbf{P}^{(1)}(\mathbf{k}, \omega) = \chi^{(1)}(\mathbf{k}, \omega) \cdot \mathbf{E}(\mathbf{k}, \omega) \quad (2.9)$$

$$\mathbf{P}^{(2)}(\mathbf{k}, \omega) = \chi^{(2)}(\mathbf{k} = \mathbf{k}_p + \mathbf{k}_q, \omega = \omega_p + \omega_q) : \mathbf{E}(\mathbf{k}_p, \omega_p) \mathbf{E}(\mathbf{k}_q, \omega_q) \quad (2.10)$$

$$\mathbf{P}^{(3)}(\mathbf{k}, \omega) = \chi^{(3)}(\mathbf{k} = \mathbf{k}_p + \mathbf{k}_q + \mathbf{k}_r, \omega = \omega_p + \omega_q + \omega_r) : \mathbf{E}(\mathbf{k}_p, \omega_p) \mathbf{E}(\mathbf{k}_q, \omega_q) \mathbf{E}(\mathbf{k}_r, \omega_r) \quad (2.11)$$

This is the polarization expressed in terms of its (familiar) linear component and its nonlinear components.

The polarization on a microscopic level describes the oscillatory response of the dipoles in the medium to the incoming electric field. The $\chi^{(i)}$'s are known as the susceptibility tensors, they characterise the optical properties of the medium. If $\chi^{(n)}$ is known for a particular n it is possible to describe the n^{th} order optical effect. The susceptibility tensors are related to the microscopic structure of the medium and quantum mechanical calculations are needed in order to derive them. $\chi^{(n)}$ is a tensor of rank n . For example one of the components of the second order polarization can be expressed by

$$P_i^{(2)} = \sum_{jk} \sum_{(pq)} \chi_{ijk}^{(2)}(\omega = \omega_p + \omega_q) E_j(\omega_p) E_k(\omega_q). \quad (2.12)$$

due to the electric dipole approximation $\chi^{(n)}(\mathbf{k}, \omega)$ becomes independent of \mathbf{k} and the electric fields become scalars since we are working with the component of the polarization. The nonlinear susceptibilities are central in the understanding of nonlinear optical effects and their derivation is shown in section 2.3. As an example consider a monochromatic plane wave incident on a nonlinear material with non zero $\chi^{(2)}$, by inserting the expression for the monochromatic plane wave

$$\mathbf{E}(\mathbf{k}, \omega) = \mathbf{E}(\mathbf{k}) \exp(i\omega t) + \text{complex conjugate} \quad (2.13)$$

into equation 2.10 the second order polarization, which is responsible for second harmonic generation, can be loosely evaluated yielding

$$\mathbf{P}^{(2)}(\mathbf{k}, \omega) = 2\chi^{(2)} \mathbf{E}(\mathbf{k}) \mathbf{E}^*(\mathbf{k}) + \chi^{(2)} \mathbf{E}^2(\mathbf{k}) \exp(2i\omega t) + \text{complex conjugate} \quad (2.14)$$

where $\mathbf{E}^*(\mathbf{k})$ refers to the complex conjugate of $\mathbf{E}(\mathbf{k})$. The atoms are polarized in such a way that they oscillate at twice the incoming frequency as is reflected in the $\exp(2i\omega t)$ term in expression 2.14. The first term in equation 2.14 leads to a process known as optical rectification. It does not lead to the generation of electromagnetic radiation because its second time derivative vanishes. Likewise the third harmonic is due to the response of the material to oscillate at three times the incoming frequency. It is important to note that no energy is transferred from the light source to the material, these nonlinear processes are completely parametric, the initial and final quantum mechanical states of the particles within the medium are identical.

2.2 Light Propagation in a Nonlinear Material

2.2.1 Coupled Waves in a Nonlinear Medium

Consider the case of second harmonic generation, there is a field with frequency ω_1 incident on a nonlinear material with non-zero $\chi^{(2)}$. The incoming field causes each atom of the nonlinear material to form an oscillating dipole, and due to a non-linearity in the atomic response this oscillating dipole has a component oscillating at twice the frequency $\omega_2 = 2\omega_1$. Each atom then produces radiation in the form of dipole radiation, frequency ω_2 is present in this dipole radiation as well as the original incident frequency. If all the individual dipoles are oscillating with a fixed phase relationship the dipole radiation they produce at frequency ω_2 will interfere constructively in the forward direction resulting in a well defined second harmonic beam. The radiation or electric field at frequency ω_2 is thus dependent on the second order nonlinear polarization which is in turn dependent on $\chi^{(2)}$ and the incident electric field as can be seen from equation 2.10. The two waves at ω_1 and ω_2 are therefore coupled through the second order nonlinear polarization and through this coupling energy is transferred back and forth between the waves.

The starting point in order to formalise this model mathematically is to consider the wave incident on the nonlinear material to be a plane wave,

$$\mathbf{E}(\mathbf{k}_i, \omega_i) = \hat{\mathbf{a}}_i A_i(z) \exp(i(\mathbf{k}_i z - \omega_i t)) \quad (2.15)$$

where $\hat{\mathbf{a}}$ is the polarization vector, $A(z)$ is the amplitude of the wave and the waves are propagating in the z direction, the subscript i runs from 1 to 2. Equation 2.15 is inserted into the nonlinear wave equation, equation 2.5. The result is two coupled wave equations, in general for an n^{th} order effect there are $n + 1$ coupled wave equations. For the case considered here the couple wave equations are thus,

$$\nabla^2 \mathbf{E}(\mathbf{k}_i, \omega_i) - \frac{n^2}{c^2} \frac{d^2 \mathbf{E}(\mathbf{k}_i, \omega_i)}{dt^2} = \frac{4\pi}{c^2} \frac{d^2 \mathbf{P}^{(2)}(\mathbf{k}_i, \omega_i)}{dt^2} \quad (2.16)$$

for $i = 1$ and $i = 2$. Substituting the relevant expression for $\mathbf{P}^{(2)}$ from equation 2.10 and calculating the time derivatives yields

$$\nabla^2 \mathbf{E}(\mathbf{k}_1, \omega_1) - \frac{n^2 \omega_1^2}{c^2} \mathbf{E}(\mathbf{k}_1, \omega_1) = \frac{4\pi \omega_1^2}{c^2} \chi^{(2)}(\omega_1) \mathbf{E}(\mathbf{k}_2, \omega_2) \mathbf{E}^*(\mathbf{k}_1, \omega_1) \quad (2.17)$$

$$\nabla^2 \mathbf{E}(\mathbf{k}_2, \omega_2) - \frac{n^2 \omega_2^2}{c^2} \mathbf{E}(\mathbf{k}_2, \omega_2) = \frac{4\pi \omega_2^2}{c^2} \chi^{(2)}(\omega_2) \mathbf{E}(\mathbf{k}_1, \omega_1) \mathbf{E}(\mathbf{k}_1, \omega_1) \quad (2.18)$$

Photon energy is conserved through the relation $\omega_2 = \omega_1 + \omega_1$. Satisfying the momentum conservation relation $\mathbf{k}_2 = \mathbf{k}_1 + \mathbf{k}_1$ maximises the coupling and thus the energy transfer between the waves. This condition is known as phase matching and is discussed in detail in section 2.5. Solving the coupled wave equations analytically is sometimes not possible, there are however certain approximations that can be made to aid us in finding a solution these will be discussed in the next subsection and detailed solutions to the coupled wave equations for second and third harmonic generation is given in section 2.4.

2.2.2 The Slowly Varying Amplitude Approximation

The coupled amplitude equations (2.17 and 2.18) are second order differential equations, but the slowly varying amplitude approximation reduces them to first order coupled differential equations thus making it easier to solve them. The amplitudes of the waves involved in a nonlinear interaction change during propagation due to the energy transfer among the waves [1]. The energy transfer only becomes significant after the waves have traveled a distance much longer than their wavelengths. In other words the relative change in the amplitude per wavelength of the waves is small. The reason for this is because the nonlinear susceptibility is much smaller than the linear susceptibility [3]. Mathematically stated the slowly varying amplitude approximation is

$$\frac{\partial^2 A}{\partial z^2} \ll k \frac{\partial A}{\partial z} \quad (2.19)$$

There are other approximations that are used to make the calculations of the coupled amplitude equations easier to solve these include the constant pump intensity approximation and the infinite plane wave approximation. Throughout this chapter the incoming and outgoing waves are considered to be infinite plane waves. This greatly simplifies the calculations although it is not strictly speaking correct. Usually the beam is focused into the nonlinear medium to increase its intensity thereby making the plane wave approximation inaccurate. Finally the constant pump intensity approximation allows one to treat the amplitudes of the incoming waves as constants. This approximation is fairly accurate for third harmonic generation since very few incoming photons are actually converted we

thus rely on sensitive measuring equipments to detect the generated photons. Second harmonic generation however is a much more efficient process. Efficiency of 81% has been achieved [7] and the constant pump intensity approximation cannot be used to solve the coupled amplitude equations.

2.3 Nonlinear Susceptibility

2.3.1 Derivation of the Nonlinear Susceptibilities using the Schrödinger Formalism.

From equation 2.14 it is clear that the magnitude of the second harmonic frequency is proportional to the second order susceptibility $\chi^{(2)}$ as well as the square of the incident electric field. The susceptibilities are characteristic of the medium and determine whether or not the material is suitable for use as a nonlinear medium. There are a number of ways of deriving expressions for the nonlinear susceptibilities: the classical approach (based on the Lorentz model of an atom) and two quantum mechanical approaches, the Schrödinger equation and the density matrix formalism [6]. The density matrix formalism yields the most complete expressions for the nonlinear susceptibilities including the description of relaxation processes such as collisional broadening. The classical model provides one with valuable insight into the structure of the medium yet it only makes provision for one resonance frequency to each atom. The Schrödinger equation approach falls midway between the classical approach and the density matrix formalism. It has the advantage of a fairly easy calculation but it fails to describe the relaxation processes that can take place. It does however provide one with a clear picture of the underlying physics in the nonlinear interaction. This section is thus devoted to the calculation of the second and third order nonlinear susceptibilities using the Schrödinger formalism.

We begin with the atomic wave function $\psi(\mathbf{r}, t)$ of the atom of the nonlinear medium, which is a solution to the time dependent Schrödinger equation

$$i\hbar \frac{\partial \psi}{\partial t} = \hat{H} \psi \quad (2.20)$$

$$\hat{H} = \hat{H}_0 + \hat{V}(t) \quad (2.21)$$

where \hat{H}_0 is the Hamiltonian for the unperturbed atom and $\hat{V}(t)$ is the interac-

tion Hamiltonian, in this case the atom is interacting with an electromagnetic field. We take it to have the form

$$\widehat{V}(t) = -\widehat{\mu} \cdot \mathbf{E}(t) \quad (2.22)$$

where $\widehat{\mu}$ is the electric dipole moment operator. When $\widehat{H} = \widehat{H}_0$ the Schrödinger equation reduces to the case of the unperturbed atom. The solution to this equation for the unperturbed atom is known and is given by

$$\psi_n(\mathbf{r}, t) = u_n(\mathbf{r}) \exp(-i\omega_n t) \quad (2.23)$$

The wave function has been separated into a spatially varying part, $u_n(\mathbf{r})$ and a time varying part, $\exp(-i\omega_n t)$. If equation 2.23 is inserted into the Schrödinger equation for the unperturbed atom, it is found that the spatially varying functions must obey the eigenvalue equation

$$\widehat{H}_0 u_n(\mathbf{r}) = E_n u_n(\mathbf{r}) \quad (2.24)$$

The spatial solutions form a complete orthonormal set, so that any solution to the Schrödinger equation can be written in terms of these functions. One of the properties of the elements of an orthonormal set is that they obey the following condition:

$$\int u_m^* u_n d^3r = \delta_{mn} \quad (2.25)$$

The Schrödinger equation for the interaction of an atom with an electric field cannot be solved exactly, it can however be solved by treating the interaction as a perturbation. The interaction Hamiltonian is modified somewhat by introducing a factor λ into equation 2.21. λ varies from zero to one and is an indication of how strong the perturbation is; $\lambda = 1$ giving the full interaction.

$$\widehat{H} = \widehat{H}_0 + \lambda \widehat{V}(t) \quad (2.26)$$

A solution to ψ in the form of a power series in λ is attempted.

$$\psi(\mathbf{r}, t) = \psi^{(0)}(\mathbf{r}, t) + \lambda \psi^{(1)}(\mathbf{r}, t) + \lambda^2 \psi^{(2)}(\mathbf{r}, t) + \dots \quad (2.27)$$

This solution to the Schrödinger equation, with the new modified interaction Hamiltonian, equation 2.26, must be a solution for any value of λ . Thus the terms proportional to the different powers of λ should satisfy the equation sep-

arately. Making use of this property yields a set of equations

$$i\hbar \frac{\partial \psi^{(0)}}{\partial t} = \widehat{H}_0 \psi^{(0)} \quad (2.28)$$

$$i\hbar \frac{\partial \psi^{(N)}}{\partial t} = \widehat{H}_0 \psi^{(N)} + \widehat{V} \psi^{(N-1)} \text{ for } N = 1, 2, 3, \dots \quad (2.29)$$

Equation 2.28 is simply the Schrödinger equation for the unperturbed atom. If the assumption is made that the atom is in some known state called the ground state then the solution to this equation is

$$\psi^{(0)}(\mathbf{r}, t) = u_g(\mathbf{r}) \exp(-iE_g t/\hbar). \quad (2.30)$$

As was mentioned earlier the spatially varying functions form a complete orthonormal basis and thus any function that is a solution to this Schrödinger equation can be written as a linear combination of these eigenfunctions. This characteristic leads to a solution to the remaining equations

$$\psi^{(N)}(\mathbf{r}, t) = \sum_l a_l^{(N)}(t) u_l(\mathbf{r}) \exp(-i\omega_l t). \quad (2.31)$$

$a_l^{(N)}(t)$ is the probability amplitude to N^{th} order in the perturbation that the atom is in state l at time t . If equation 2.31 is substituted into equation 2.29 it is possible to relate all the probability amplitudes of order N to all of the probability amplitudes of order $N-1$:

$$i\hbar \sum_l \frac{da_l^{(N)}}{dt} u_l(\mathbf{r}) \exp(i\omega_l t) = \sum_l a_l^{(N-1)} \widehat{V} u_l(\mathbf{r}) \exp(i\omega_l t) \quad (2.32)$$

This equation can be simplified by again making use of the orthonormal characteristic of the spatially varying functions $u_l^N(\mathbf{r})$. Multiply both sides of the equation from the left hand side by u_m^* and integrate over all space to obtain

$$\frac{da_l^{(N)}}{dt} = (i\hbar)^{-1} \sum_l a_l^{(N-1)} \widehat{V}_{ml} \exp(i\omega_{ml} t) \quad (2.33)$$

with

$$\omega_{ml} = \omega_m - \omega_l \quad (2.34)$$

and

$$\widehat{V}_{ml} = \int u_m^* \widehat{V} u_l d^3r. \quad (2.35)$$

By time integration of the right hand side of equation 2.33 it is possible to determine the probability amplitude of order N , provided that the probability amplitude of order $N - 1$ is known. This is thus a stepwise procedure that allows for the calculation of all the probability amplitudes. Since it is assumed that the atom is in some initial ground state g , the probability amplitude $a_g^{(0)}$ is then known, from here it is possible to determine the probability amplitude of the next highest order and so forth. Equation 2.33 is integrated with respect to time, in the integration it is assumed that the contribution from the lower limit vanishes.

$$a_m^{(N)} = (i\hbar)^{-1} \sum_l \int_{-\infty}^t dt' V_{ml}(t') a_l^{(N-1)}(t') \exp(i\omega_{ml}t') \quad (2.36)$$

The atom is assumed to be in an initial well defined state, its ground state, because of this condition the first amplitude is simply a delta function.

$$a_l^{(0)} = \delta_{gl} \quad (2.37)$$

The nonlinear susceptibilities are related to these probability amplitudes through the nonlinear polarization. The contributions to the nonlinear polarization can be expressed in terms of the induced dipole moment. For example the second order polarization can be expressed as;

$$\mathbf{P}^{(2)} = N \langle \mathbf{p}^{(2)} \rangle \quad (2.38)$$

Where $\langle \mathbf{p}^{(2)} \rangle$ is the second order contribution to the induced atomic dipole moment. $\langle \mathbf{p}^{(2)} \rangle$ is related to the wave function equation 2.27

$$\langle \mathbf{p}^{(2)} \rangle = \langle \psi^{(0)} | \widehat{\mu} | \psi^{(2)} \rangle + \langle \psi^{(1)} | \widehat{\mu} | \psi^{(1)} \rangle + \langle \psi^{(2)} | \widehat{\mu} | \psi^{(0)} \rangle \quad (2.39)$$

The wave functions are related to the probability amplitudes via equation 2.31. To solve for the second order contribution to the induced atomic dipole moment expressions for the probability amplitudes $a_m^{(1)}(t)$ and $a_n^{(2)}(t)$ are needed. By inserting equation 2.37 into equation 2.36 it is possible to determine $a_m^{(1)}(t)$ and then $a_n^{(2)}(t)$ and so forth, for the full expressions see [6]. These expressions are then inserted into equation 2.31 to determine the wave functions. The

wave functions are then inserted into equation 2.39 to determine the atomic dipole moment. Equation 2.39 is then inserted into equation 2.38 to obtain an expression for the polarization which is then compared to equation 2.12 to obtain an expression for the susceptibility. The expressions for the the second and third order nonlinear susceptibilities are reproduced and discussed below. For a derivation in the manner described see [6] and for a more thorough approach see Armstrong *et al* [3]. Expression 2.40 is a simplified expression for the second order susceptibility,

$$\chi_{ijk}^{(2)}(\omega_p + \omega_q; \omega_p, \omega_q) = \frac{N}{\hbar^2} P_I \left(\frac{\mu_{gn}^i \mu_{nm}^j \mu_{mg}^k}{(\omega_{ng} - \omega_p - \omega_q)(\omega_{mg} - \omega_p)} + \frac{\mu_{gn}^j \mu_{nm}^i \mu_{mg}^k}{(\omega_{ng} + \omega_q)(\omega_{mg} - \omega_p)} + \frac{\mu_{gn}^j \mu_{nm}^k \mu_{mg}^i}{(\omega_{ng} + \omega_q)(\omega_{mg} + \omega_p + \omega_q)} \right) \quad (2.40)$$

where μ_{gn}^i is the electric dipole transition moment and P_I is the intrinsic permutation operator. Expression 2.40 actually comprises of 6 terms but due to the intrinsic permutation operator P_I it is possible to express it in this form [6]. The other three terms are obtained by simultaneous permutation of the frequencies and the Cartesian coordinates, i, j and k . In the summation over the excited levels m and n the only levels that contribute are those that obey the selection rules for electric dipole transitions [6]. In a similar manner it is possible to derive an expression for the third order susceptibility. It consists of a total of 24 terms when derived using this formalism; again due to the intrinsic permutation operator it is only necessary to show four terms

$$\begin{aligned} & \chi_{ijkl}^{(3)}(\omega_p + \omega_q + \omega_r) \\ = & \frac{N}{\hbar^3} P_I \sum mnv \left[\frac{\mu_{gv}^k \mu_{vn}^j \mu_{nm}^i \mu_{mg}^h}{(\omega_{vg} - \omega_r - \omega_q - \omega_p)(\omega_{ng} - \omega_q - \omega_p)(\omega_{mg} - \omega_p)} \right. \\ & + \frac{\mu_{gv}^j \mu_{vn}^k \mu_{nm}^i \mu_{mg}^h}{(\omega_{vg} + \omega_r)(\omega_{ng} - \omega_q - \omega_p)(\omega_{mg} - \omega_p)} \\ & + \frac{\mu_{gv}^j \mu_{vn}^i \mu_{nm}^k \mu_{mg}^h}{(\omega_{vg} + \omega_r)(\omega_{ng} + \omega_r + \omega_q)(\omega_{mg} - \omega_p)} \\ & \left. + \frac{\mu_{gv}^j \mu_{vn}^i \mu_{nm}^h \mu_{mg}^k}{(\omega_{vg} + \omega_r)(\omega_{ng} + \omega_r + \omega_q)(\omega_{mg} + \omega_r + \omega_q + \omega_p)} \right] \quad (2.41) \end{aligned}$$

2.3.2 Resonant Enhancement

The magnitude of certain elements of the nonlinear susceptibilities can be enlarged by tuning the incident radiation to a certain frequency, this is known as resonant enhancement. In theory it is possible to enhance all orders of the nonlinear susceptibilities but in practice it is used especially when doing third

harmonic generation in gaseous media. While gaseous media have small $\chi^{(3)}$'s, with resonant enhancement it is possible to increase the magnitudes of the elements of $\chi^{(3)}$ and make the third order effects more pronounced. The energy levels of free atoms are extremely sharp; if the radiation incident upon the gaseous medium is tuned to almost coincide to one of these resonances certain terms in the expression for the nonlinear susceptibility 2.41 become extremely large. The coupling between the radiation and the atom becomes very strong, the polarization is enhanced, the amplitudes of the oscillating dipoles enlarged and the efficiency of the third order process is increased. The possibilities for resonance is characterised by the nonlinear susceptibility, for example the possible resonances in the case of third harmonic generation as described by 2.41 are illustrated in figure 2.1. Two types of processes occur single resonances (one photon resonance), where one photon is tuned close to an energy level and double resonances (two-photon resonance), where the sum of two photons is tuned to a resonance. In reality the singly resonant cases lead to linear absorption of the fundamental or generated beam and are thus not suitable to enhance third order effects. The two photon absorption cross section of gaseous media is in general small and there is little absorption that takes place in the two photon resonant case. This is used for resonant enhancement. Depending on

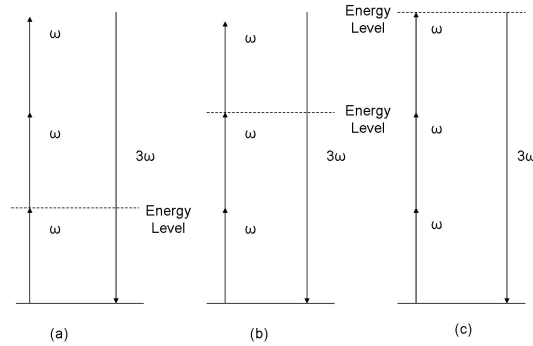


Figure 2.1: (a) and (c) illustrate the one photon resonant case where the frequency of one of the photons is tuned close to a dipole allowed transition frequency. (b) shows the two photon resonance where the sum of the frequencies of two photons is tuned close to a transition frequency.

the nonlinear material's energy level structure it may have more than one useful

two photon resonance. For example zinc has three two photon resonances as discussed in section 2.6.

2.3.3 Symmetry Properties of the Nonlinear Susceptibilities

Symmetry relations greatly reduce the number of independent elements in the nonlinear optical susceptibilities tensors. In order to completely characterise the second order polarization as given by equation 2.10 the following components of the susceptibility tensor need to be found with the constraint that $\omega_p + \omega_q = \omega_{p+q}$.

$$\begin{aligned} \chi_{ijk}^{(2)}(\omega_p, \omega_{p+q}, -\omega_q); & \quad \chi_{ijk}^{(2)}(\omega_p, -\omega_q, \omega_{p+q}) \\ \chi_{ijk}^{(2)}(\omega_q, \omega_{p+q}, -\omega_p); & \quad \chi_{ijk}^{(2)}(\omega_q, -\omega_p, \omega_{p+q}) \\ \chi_{ijk}^{(2)}(\omega_{p+q}, \omega_p, \omega_q); & \quad \chi_{ijk}^{(2)}(\omega_{p+q}, \omega_q, \omega_p) \end{aligned} \quad (2.42)$$

There are in effect twelve that need to be found since each frequency can be replaced by its negative. Still more need to be found since the indices i, j and k can take on the Cartesian coordinate x, y and z independent of each other. Thus each of the twelve components actually consist of 27 Cartesian components leaving a total of 324 components that need to be specified in order to completely characterise the second order polarization. With symmetry relations it is possible to reduce this number by only specifying the independent components. In equation 2.40 and 2.41 P_I represents the intrinsic permutation operator, it can be used because these expressions display intrinsic permutation symmetry.

2.3.3.1 Intrinsic Permutation Symmetry

One of the contributions to the second order nonlinear polarization is

$$\chi_{ijk}^{(2)}(\omega_{p+q}, \omega_q, \omega_p) \quad (2.43)$$

again with the constraint that $\omega_p + \omega_q = \omega_{p+q}$. By exchanging pairs of indices p, k and q, j there should be no change in the value of this component. The

indices p, k, q, j and i are simply place holders. Thus

$$\chi_{ijk}^{(2)}(\omega_{p+q}, \omega_q, \omega_p) = \chi_{ikj}^{(2)}(\omega_{p+q}, \omega_p, \omega_q) \quad (2.44)$$

This is known as intrinsic permutation symmetry. The operator P_I in equations 2.40 averages the expression over both permutations of the frequencies ω_p and ω_q . The Cartesian coordinates j and k are permuted together with the frequencies. Similarly in equation 2.41 the operator averages over permutations of all three frequencies ω_p, ω_q and ω_r . Again the Cartesian coordinates j, k and l permute with their respective frequencies.

2.3.3.2 Lossless Media

Under certain circumstances a nonlinear medium can be considered lossless. Lossless media possess full permutation symmetry. This arises from the fact that all the tensor components of a lossless medium are real. It is possible to verify this by evaluating the full quantum mechanical expressions of the tensors at frequencies that are far from a resonance [6]. Full permutation symmetry implies that any pair of frequency arguments can be exchanged provided that their Cartesian coordinates are exchanged with them and the condition set on the frequencies is not violated. For example with full permutation symmetry;

$$\chi_{ijk}^{(2)}(\omega_{p+q}, \omega_q, \omega_p) = \chi_{jki}^{(2)}(\omega_p, -\omega_q, \omega_{p+q}) \quad (2.45)$$

2.3.3.3 Spatial Symmetries

Spatial symmetries of the medium are reflected in the nonlinear susceptibilities. Some tensor components might be zero and others might be related to each other due to the structural symmetries of the medium. This is relevant in crystalline media such as Beta Barium Borate (BBO) which is a crystal that is able to frequency double radiation from 409.6 - 3500 nm [8]. For example consider a crystal with x and y directions identical. Rotations of 90 degrees around the z-axis will result in no change in structure thus optical responses for applied

fields in the x and y direction would be the same resulting in

$$\chi_{zxx}^{(2)} = \chi_{zyy}^{(2)} \quad (2.46)$$

For a specific crystal, it is possible to determine the form of the linear and nonlinear susceptibilities by making use of its symmetry properties. Crystals are classified into one of 32 possible crystal classes. These crystal classes are derived using group theory and symmetry operations. For a full discussion see [9].

2.4 The Coupled Wave Equations

2.4.1 The Coupled Wave Equations for Second Harmonic Generation

A mathematical description of the second harmonic generation as illustrated in figure 2.2 process leads to an important feature of nonlinear processes, that of phase matching. In the brief description given, the most important features are summarised from the treatment of second harmonic generation by Robert W. Boyd [6]. A much more thorough treatment is given by Armstrong *et al* [3]. In this description it is assumed that the medium is lossless at the fundamental frequency and the second harmonic frequency. The electric fields are assumed to propagate in the z-direction only, thus the \mathbf{k} vectors can be treated as scalars in the calculation. The total electric field propagating through the nonlinear medium is

$$\mathbf{E}(z, t) = \mathbf{E}_1(z, t) + \mathbf{E}_2(z, t) \quad (2.47)$$

where

$$\mathbf{E}_j(z, t) = \mathbf{E}_j(z) \exp(-i\omega_j t) + \text{complex conjugate} \quad (2.48)$$

and

$$\mathbf{E}_j = A_j \exp(ik_j z) \quad (2.49)$$

The wave number k_j is given by

$$k_j = \frac{n_j \omega_j}{c} \quad (2.50)$$

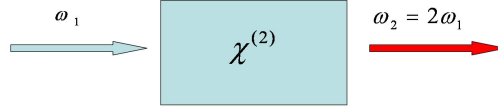


Figure 2.2: Second Harmonic Generation

with n_j representing the refractive index of the radiation.

We assume that each frequency component satisfies equation 2.5. The tensor

$$d_{ijk} = \frac{1}{2}\chi_{ijk}^{(2)} \quad (2.51)$$

is introduced. The second order nonlinear polarization, responsible for second harmonic generation, is given by equation 2.10. For fixed propagation and polarization directions of the incoming radiation it reduces to the scalar relationship

$$P(2\omega) = 2d_{eff}E(\omega)^2 \quad (2.52)$$

where

$$E(\omega) = \left[\sum_j E_j(\omega)^2 \right]^{\frac{1}{2}} \quad (2.53)$$

d_{ijk} reduces to d_{eff} for fixed propagation and polarization directions by evaluating the summation Σ_{jk} in equation 2.10 [10].

It is now possible to evaluate the nonlinear wave equation, 2.5. The differentiation follows fairly easily and is an application of the product rule for differentiation. The ∇^2 reduces to $\frac{\partial^2}{\partial z^2}$ since wave propagation is considered in the z -direction only. The slowly varying amplitude approximation reduces the equations to first order differential equations as discussed in section 2.2.2. A wave equation is evaluated for each frequency component and the results are

$$\frac{dA_1}{dz} = \frac{8i\pi\omega_1^2}{k_1c^2}d_{eff}A_2A_1^*\exp(i\Delta kz) \quad (2.54)$$

$$\frac{dA_2}{dz} = \frac{4i\pi\omega_1^2}{k_2c^2}d_{eff}A_1^2 \exp(i\Delta kz) \quad (2.55)$$

where

$$\Delta k = 2k_1 - k_2 \quad (2.56)$$

and is known as the wave vector mismatch. To solve the pair of coupled equations it is easier to work with the modulus and phase of each field amplitude and to express these amplitudes in dimensionless form [6]. The complex slowly varying amplitudes are expressed as

$$A_1 = \left(\frac{2\pi I}{n_1c}\right)^{\frac{1}{2}}u_1 \exp(i\phi_1) \quad (2.57)$$

$$A_2 = \left(\frac{2\pi I}{n_2c}\right)^{\frac{1}{2}}u_2 \exp(i\phi_2) \quad (2.58)$$

The total intensity of the waves is introduced

$$I = I_1 + I_2 \quad (2.59)$$

where the individual intensities are given by the usual expression

$$I_k = \frac{n_kc}{2\pi} |A_k|^2 \quad (2.60)$$

A normalised distance parameter is introduced

$$\zeta = z/l \quad (2.61)$$

where

$$l = \left(\frac{n_1^2n_2c^3}{2\pi I}\right)^{\frac{1}{2}} \frac{1}{8\pi\omega_1d_{eff}} \quad (2.62)$$

is the characteristic distance over which the fields exchange energy [6]. A normalised wave vector mismatch

$$\Delta s = \Delta kl \quad (2.63)$$

as well as the relative phase of the interacting fields

$$\theta = 2\phi_1 - \phi_2 + \Delta kz$$

are also introduced. After the insertion of the quantities u_k, ϕ_k, ζ and Δs into the coupled amplitude equations 2.57 and 2.58 and some algebraic manipulation

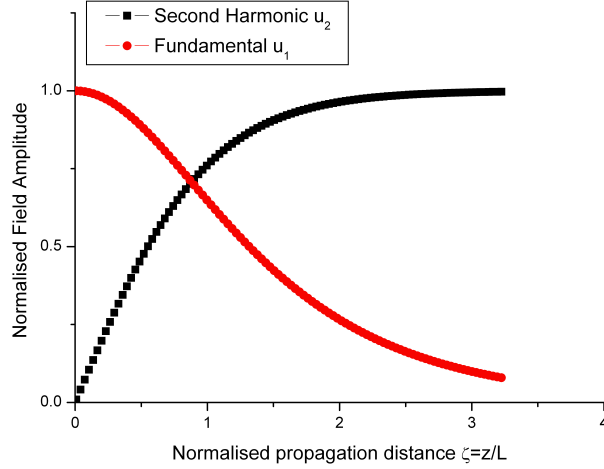


Figure 2.3: The solutions to the coupled differential equations for second harmonic generation.

the result is a set of coupled differential equations for the three quantities u_1 , u_2 and θ . For the full equations see [6]. When $\Delta k = 0$ we have the case of perfect phase matching, the solution to the coupled amplitude equations in this instance are

$$u_1(\zeta) = \operatorname{sech}(\zeta) \quad (2.64)$$

$$u_2(\zeta) = \tanh(\zeta) \quad (2.65)$$

here it is assumed that $u_2(0) = 0$ and $u_1(0) = 1$. Which is the physically real situation that no second harmonic light is incident on the nonlinear material. These solutions are illustrated graphically in figure 2.3 . The solutions to the coupled amplitude equations for any value of Δk can be expressed in terms of elliptic integrals [3]. Phase matching in a BBO crystal and a metal vapour is discussed in more detail in section 2.5.

2.4.2 The Coupled Wave Equations for Third Harmonic Generation

The coupled amplitude equations for third harmonic generation are derived

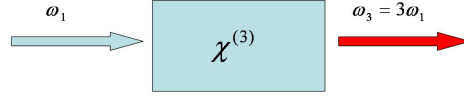


Figure 2.4: Third Harmonic Generation

in much the same fashion as those for second harmonic generation. The difference is that there are four waves interacting instead of three and it is the third order nonlinear polarization that is responsible for the component at frequency three times that of the incoming, the process is visualised in figure 2.4.

The coupled amplitude equations for third harmonic generation are thus given by

$$\frac{\partial A_3}{\partial z} = \frac{2i\pi\omega_1^2}{k_3c^2}\chi^{(3)}(\omega_3)A_1^3 \exp(-iz\Delta k) \quad (2.66)$$

$$\frac{\partial A_1}{\partial z} = \frac{6i\pi\omega_1^2}{k_1c^2}\chi^{(3)}(\omega_1)A_1^*A_1^*A_3 \exp(-iz\Delta k) \quad (2.67)$$

where

$$\Delta k = 3k_1 - k_3 \quad (2.68)$$

Since $|\chi^{(3)}| \ll |\chi^{(2)}|$ conversion efficiencies for the third harmonic are much lower than for the second harmonic. In the order of 1×10^{-6} for input powers of 1kW [4]. The undepleted pump approximation is therefore valid and amplitude A_1 is considered to be a constant. Considering the condition of perfect phase matching, $\Delta k = 0$, the amplitude A_3 increases linearly with z . The intensity of the third harmonic radiation therefore increases quadratically with z according to equation 2.60. When the case of perfect phase matching is not satisfied the intensity of the third harmonic wave increases more slowly with z . The coupled amplitude equations for third harmonic generation are solved in detail by Armstrong *et al* [3]. From the argument presented here and in subsection

2.4.1 it is clear that phase matching plays an important role in the efficiency of the nonlinear process.

2.4.3 The Coupled Wave Equations for Four Photon Sum Frequency Generation

In order to describe the four photon sum frequency generation process,

$$\omega_3 = \omega_1 + \omega_1 + \omega_2 \quad (2.69)$$

the medium cannot be described as lossless since the the sum frequency wave is in the VUV and can be absorbed by the metal vapour medium. For this case the fundamental equation of nonlinear optics takes on a slightly different form. An extra term is included in the coupled wave equations that describe the attenuation of the wave due to one-photon absorption with an absorption cross section $\sigma(\omega)$. The incident optical fields are again described by equation 2.15. The slowly varying amplitude approximation is applicable so that the second order time derivative can be neglected. The result for ω_3 is

$$\frac{dA_3(z)}{dz} = \frac{i6\pi\omega_3^2}{k_3c^2}\chi^{(3)}(\omega_3, \omega_2, \omega_1, \omega_1)A_2(z)[A_1(z)]^2 \exp(i\Delta kz) - \frac{\sigma(\omega_3)N}{2}A_3(z) \quad (2.70)$$

where N is the number density of the medium and $\Delta k = (2k_1 + k_2) - k_3$. Conversion efficiencies for four wave sum frequency mixing are of the order of 1×10^{-6} and therefore the undepleted pump approximation can be used. The amplitudes may be affected by the one photon absorption in the medium, their expressions are given by

$$A_1(z) = A_1(z=0) \exp\left(\frac{-N\sigma(\omega_1)z}{2}\right) \quad (2.71)$$

$$A_2(z) = A_2(z=0) \exp\left(\frac{-N\sigma(\omega_2)z}{2}\right) \quad (2.72)$$

After inserting equations 2.71 and 2.72 into equation 2.70

$$\begin{aligned} \frac{dA_3(z)}{dz} = & \\ & \frac{i6\pi\omega_3^2}{k_3c^2}\chi^{(3)}(\omega_3, \omega_2, \omega_1, \omega_1)A_2(0)[A_1(0)]^2 \times \\ & \exp(i\Delta kz) \exp\left(-N\frac{(2\sigma_1+\sigma_2)}{2}\right) - \frac{\sigma(\omega_3)N}{2}A_3(z) \end{aligned} \quad (2.73)$$

is obtained. With the assumption that the density stays constant over the whole length of the medium and is zero outside its length L , equation 2.73 is

integrated with respect to z from 0 to L yielding

$$A_3(L) = \frac{i6\pi\omega_3^2}{k_3c^2} L \chi^{(3)}(\omega_3, \omega_2, \omega_1, \omega_1) A_2(0) [A_1(0)]^2 \times \frac{\exp(-\Gamma_3/2)}{(\Gamma_3 - \Gamma_i)/2 + i\Delta kL} (\exp((\Gamma_3 - \Gamma_i)/2 + i\Delta kL) - 1) \quad (2.74)$$

where the absorption cross sections have been rewritten in the form of optical depths. $\Gamma_3 = \sigma(\omega_3)NL$ is the optical depth of the medium at ω_3 and $\Gamma_i = 2\Gamma_1 + \Gamma_2 = [2\sigma(\omega_1) + \sigma(\omega_2)]NL$ is the optical depth at the two incident frequencies. The intensity of the sum frequency is again defined by equation 2.60 yielding

$$I_3(L) = \frac{144\pi^4\omega_3^2}{n_2n_1^2n_3c^4} L^2 [\chi^{(3)}(\omega_3, \omega_2, \omega_1, \omega_1)]^2 I_2(0) [I_1(0)]^2 F(\Delta k, \Gamma_i, \Gamma_3) \quad (2.75)$$

where

$$F(\Delta k, \Gamma_i, \Gamma_3) = \frac{\exp(-\Gamma_i) + \exp(-\Gamma_3) - 2\exp(-\frac{\Gamma_3 - \Gamma_i}{2}) \cos(\Delta kL)}{(\frac{\Gamma_3 - \Gamma_i}{2})^2 + (\Delta kL)^2} \quad (2.76)$$

is known as the phase matching factor. Equation 2.75 is an important equation since it demonstrates what parameters need to be optimised in order to optimise the sum frequency radiation. It illustrates that the length of the medium, the incident laser intensities, and the phase matching factor are all critical for the efficient generation of the sum frequency radiation.

For an optically thin medium $\Gamma_i = \Gamma_3 = 0$ the phase matching factor reduces to

$$F(\Delta kL) = L^2 \frac{\sin^2(\Delta kL/2)}{(\Delta kL/2)^2} \quad (2.77)$$

The phase matching factor is an oscillating function with a central peak and slowly decreasing peaks left and right of the central peak as illustrated in figure 2.5. The phase matching factor is produced in figure 2.5 for three different optical depths with the assumption that the medium is optically thin for the frequencies at ω_1 and ω_2 . This is physically possible since the incoming frequencies are in the visible and therefore transparent in the metal vapour where as the sum frequency wave is in the VUV and can be absorbed by the metal vapour medium. The larger Γ_3 becomes the more the beam at ω_3 is absorbed. As Γ_3 increases the phase matching factor tends to a Lorentzian profile. When $\Delta k = 0$ the condition of perfect phase matching is achieved

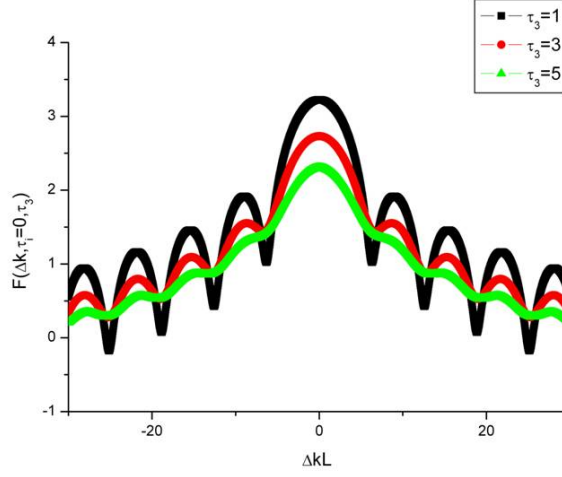


Figure 2.5: Phase matching curve for three different optical depths, assuming that the medium is optically thin for the incoming frequencies.

corresponding to the central peak in the curve. I_3 is then proportional to the square of the medium length and the incoming intensities. When $\Delta k \neq 0$ I_3 decreases with an increase in $|\Delta k|L$. This is due to the generated field becoming out of phase with the incident fields so that energy is converted back into the fields with frequencies ω_1 and ω_2 . When the length of the material is larger than $\frac{1}{|\Delta k|}$ the field with frequency ω_3 generated at the end of the medium starts to interfere destructively with the ω_3 field generated at the start of the medium resulting in a decrease in the output of the field at ω_3 .

The conversion efficiency can be increased by focusing of the incident laser beam. The plane wave approximation, used thus far, is no longer valid since a plane wave cannot describe a focused beam. A Gaussian intensity distribution is considered. The Gaussian intensity distribution has the form

$$E(r, z, t) = E(r, z) \frac{b}{b + 2iz} \exp\left(\frac{-kr^2}{b + 2iz}\right) \exp(ikz) \quad (2.78)$$

where

$$b = 2z_0 = \frac{2\pi W_0^2}{\lambda} = kW_0^2 \quad (2.79)$$

is the confocal parameter with W_0 the beam waist ($\frac{1}{e^2}$ radius of the intensity distribution) in the focal plane. The effect on the phase matching is to change

the phase matching factor. Expression 2.77 becomes dependent on the confocal parameter. The expression is given by

$$F(\Delta kL, b/L) = \frac{1}{L^2} \left[\int_{-L/2}^{L/2} \frac{\exp(-i\Delta kz)}{(1 + 2iz/b)^2} dz \right]^2 \quad (2.80)$$

Equation 2.80 reduces to equation 2.77 when $b \rightarrow \infty$.

The generation of the third harmonic of the resonant incident dye laser frequency ω_1 competes against the sum frequency generation $\omega_{sf} = \omega_1 + \omega_1 + \omega_2$. It is possible to suppress the generation of the third harmonic by polarizing the two incident beams circularly in opposite senses. The atom is in the same quantum mechanical state before and after the process so the sum of the components of the angular momenta of the four photons must add up to zero. When the incident beam at frequency ω_1 has for example positive helicity each photon carries an angular momentum component $+\hbar$. If the beam at frequency ω_2 has negative helicity it carries an angular momentum component $-\hbar$. The resultant magnitude of the angular momentum component for the third harmonic photon has to be $3\hbar$ so that the sum of the angular momentum of all four photons is zero. This violates the quantum mechanical that a photon cannot carry angular momentum component larger than \hbar . The resultant magnitude of the angular momentum of the sum frequency photon has to be \hbar which satisfies the quantum mechanical principle.

2.5 Phase Matching

Phase matching plays an important role in the output of the tripled, doubled and sum frequencies. In this section phase matching for second harmonic generation in a BBO crystal and third harmonic generation in a metal vapour will be explained in more detail.

2.5.1 Properties of the BBO Crystal

Beta Barium Borate (BBO) was the nonlinear material of choice for second harmonic generation. A few important properties of this material bear mention here. The BBO crystal is a negative uniaxial crystal which belongs to the trigonal system with a point symmetry of $3m$ [8]. It has an extremely broad phase matchable range from 409.6 to 3500 nm [8]. In the present study it was

used to frequency double tuneable dye laser radiation but due to the broad phase matching angle it is well suited to double the frequency of many other laser sources. BBO has three important traits that make it an efficient frequency doubling crystal.

1. BBO has a high damage threshold. This is due to a large bandgap making it difficult to excite electrons from the conduction band to the valence band. The damage threshold is in the order of 10 GW/cm^2 for 100 ps pulse widths, measured at the Nd:YAG wavelength of 1064 nm [8]. This makes it possible to focus the beam quite tightly into the crystal and increase the efficiency of the nonlinear process.
2. Laser induced heating of the crystal is a negligible effect on the efficiency of the nonlinear process. This is due to the index of refraction having a very low temperature dependence. The crystal has a very high melting point of 1095 degrees Celsius [8].
3. It has a large second order nonlinear susceptibility.

Conversion efficiencies as high as 81% have been achieved by Feng *et al* [7]. They doubled a Nd:YAP laser with unstable resonator. The BBO crystal was placed in the cavity of this laser and frequency doubling from 1080 to 540 nm was achieved. For the doubling of tuneable dye laser radiation a maximum conversion efficiency of 36% has been achieved at a wavelength of 619.8 nm with a power of 150 kW for 22 ns pulsewidths [8].

2.5.2 Phase Matching in a BBO Crystal

When the wave vector mismatch, Δk , is zero the condition of perfect phase matching is satisfied. This implies that the different contributions to the generated second harmonic wave in the nonlinear medium interfere constructively, so as to produce the most effective energy conversion into the second harmonic wave. Microscopically we can think of all the individual atomic dipoles as oscillating in a fixed phase relation with both the fundamental and second harmonic field, so that the fields from all dipoles add coherently in the forward direction.

The phase matching condition is essentially the conservation of linear momentum, since \mathbf{k} is related to \mathbf{p} through

$$\mathbf{k} = \frac{n\mathbf{p}}{h} \quad (2.81)$$

The phase matching condition is also related to the refractive index of the nonlinear material via equation 2.50. The phase matching condition for second harmonic generation then reduces to

$$n(\omega) = n(2\omega) \quad (2.82)$$

Phase matching for second harmonic generation is achieved in a BBO crystal by making use of the birefringence of the crystal. BBO is a negative uniaxial crystal i.e. it has one axis of symmetry known as the optic axis. Light polarized perpendicularly to the plane containing the propagation vector \mathbf{k} and the optic axis is called the ordinary ray, this light experiences a refractive index n_o . The ordinary ray travels through the nonlinear crystal with a velocity that is independent of the direction of propagation. Light polarized in the plane containing \mathbf{k} and the optic axis is called the extraordinary ray and it experiences an index of refraction $n_e(\theta)$ which is dependent on the angle between \mathbf{k} and the optic axis. $n_e(\theta)$ is given by

$$n_e(\theta) = \sqrt{\frac{\bar{n}_e^2 n_o^2}{n_o^2 \sin^2 \theta + \bar{n}_e^2 \cos^2 \theta}} \quad (2.83)$$

where $\bar{n}_e = n_e(\pi)$ is known as the principal value of the extraordinary refractive index. Equation 2.83 can be derived using Fresnel's equation of wave normals [11]. The extraordinary wave travels through the nonlinear crystal with a velocity that is dependent on the direction of propagation through the crystal [11]. If the birefringence ($n_e - n_o$) of the crystal is positive the crystal is termed positive uniaxial; if the birefringence is negative the crystal is described as negative uniaxial. BBO is negative uniaxial because $n_e(\theta) < n_o$ as is illustrated by figure 2.6. The ray direction (Poynting vector) and the wave normal (\vec{k} -vector) of the extraordinary ray do not coincide. There is a non-zero angle ρ between the Poynting vector and the \vec{k} -vector resulting in the phenomenon of "walk-off". Due to the "walk-off" angle ρ , the direction of the energy of the e-ray and the o-ray do not coincide resulting in a decoupling of the two waves over a certain distance [12]. This limits the length of the medium over which phase match-

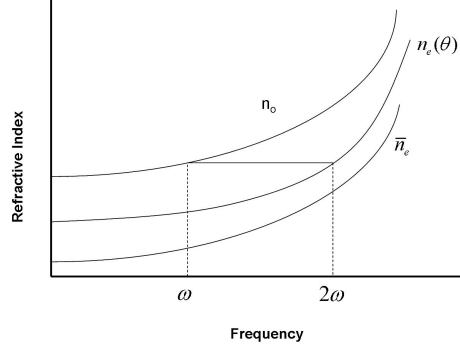


Figure 2.6: A sketch of the dependence of the refractive index on frequency for a negative uniaxial crystal. The negative refers to the fact that the extraordinary index of refraction n_e is less than the ordinary index of refraction n_o . $n_e(\theta)$ indicates the extraordinary index of refraction for which phase matching is possible for second harmonic generation.

ing is effective. BBO has a relatively small walk-off angle of 2.74 degrees and thus walk-off in crystals with lengths in the order of 1 cm does not limit phase matching [8].

As was seen from equation 2.82 the indices of refraction of the two waves need to be matched. By polarizing the doubled frequency (2ω) wave in the direction that gives it the extraordinary index of refraction and polarizing the fundamental beam (ω) in the direction that gives it the ordinary index of refraction it is possible to match the indices by changing the angle θ :

$$n_o(\omega) = n_e(2\omega, \theta) \quad (2.84)$$

with $n_e(2\omega, \theta)$ given by equation 2.83. Inserting equation 2.83 into 2.84 yields [6]

$$\theta = \arcsin\left(\frac{\bar{n}_e(2\omega)}{n_o(\omega)} \sqrt{\frac{n_o(2\omega)^2 - n_o(\omega)^2}{n_o(2\omega)^2 - \bar{n}_e(2\omega)^2}}\right) \quad (2.85)$$

This equation gives the exact propagation direction for the light in the crystal for perfect phase matching. This is known as type I phase matching [10].

2.5.3 Phase Matching in a Gaseous Medium

The condition for phase matching for third harmonic generation is

$$n(\omega) = n(3\omega) \quad (2.86)$$

For third harmonic generation in a metal vapour this can be achieved by adding another gas to the metal vapour. The phase matching gas needs to be non-reactive with the metal vapour and typically a noble gas is used. Another requirement of the two component gas system is that one of the gases needs to display anomalous dispersion ($n(3\omega) < n(\omega)$) and the other needs to display normal dispersion ($n(3\omega) > n(\omega)$) in this region. By changing the pressure ratio of the gases in the mixture it is possible to find a ratio where the refractive indices of the fundamental and the tripled frequency are matched.

Theoretically this ratio can be calculated if the real parts of the linear susceptibilities at both the fundamental and the tripled frequencies are known. The refractive indices at the different frequencies are given by

$$n(\omega) = 1 + 2\pi[N_a\alpha_a^{(1)}(\omega) + N_b\alpha_b^{(1)}(\omega)] \quad (2.87)$$

$$n(3\omega) = 1 + 2\pi[N_a\alpha_a^{(1)}(3\omega) + N_b\alpha_b^{(1)}(3\omega)] \quad (2.88)$$

where $\alpha_k^{(1)}(\omega)$ is known as the atomic polarisability and is related to the non-linear susceptibility through the equation

$$\chi_k^{(1)} = N_k\alpha_k^{(1)}(\omega) \quad (2.89)$$

with N_k the density of gas $k = a, b$ [13].

By making use of equation 2.86 equations 2.87 and 2.88 are equated to yield

$$\frac{N_a}{N_b} = \frac{\alpha_b^{(1)}(3\omega) - \alpha_b^{(1)}(\omega)}{\alpha_a^{(1)}(\omega) - \alpha_a^{(1)}(3\omega)}$$

where the ratio $\frac{N_a}{N_b}$ is equal to the pressure ratio $\frac{P_a}{P_b}$ required for phase matching.

2.6 Zinc and Magnesium Vapour as Nonlinear Media

The suitability of zinc as a nonlinear medium lies in its large two-photon, resonantly enhanced third order susceptibility, $\chi^{(3)}(3\omega) = 3.1 \times 10^{-31}$ esu/atom at 120 nm [14]. It also has several closely spaced two-photon resonances that can be reached by a combination of available dye laser frequencies. It also has a small absorption cross section $\sigma = 4 \times 10^{-20}$ cm² [14] in the spectral region just above its ionization limit at 132 nm. This makes it suitable for short wavelength generation as reported by Jamroz *et al* [14] who achieved tuneability from 140.4 to 106.3 nm. By making use of the two-photon resonance at the $5s^1S_0$ level

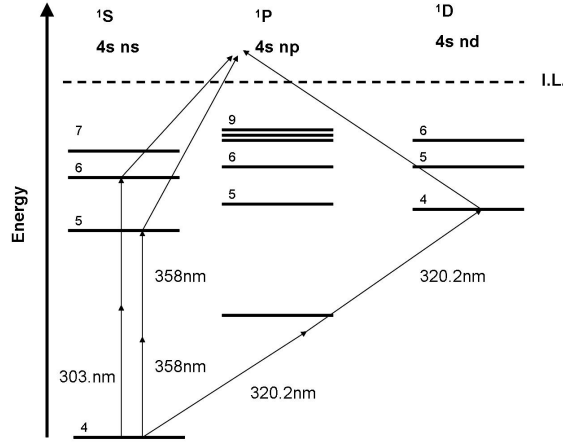


Figure 2.7: Energy level diagram of Zinc

they obtained a generation efficiency of greater than 10^{-7} for third harmonic generation. Third harmonic generation with the $4d^1D_2$ yielded a slightly lower generation efficiency of 10^{-8} . They also investigated the generation of sum frequency with the three different two photon resonances; a representation of the two-photon resonances can be seen in figure 2.7. Table 2.1 provides a summary of their results. Herman *et al* [4] reported similar findings with conversion efficiencies of between 10^{-5} and 10^{-6} in the tuning range 140 - 129 nm. Their study included a comparison between three different nonlinear materials, namely zinc, magnesium and mercury. It was reported that for similar laser intensities zinc produced on average 6^2 more photons than magnesium at 140 nm; this is due to

Two-Photon Resonance	Tuning Range	Efficiency
$5s^1S_0$ (358nm)	140nm -128nm	3×10^{-7}
$4d^1D_2$ (320.2nm)	128nm-111nm	1×10^{-8}
$6s^1S_0$ (303nm)	lower limit of 106.3nm	3×10^{-9}

Table 2.1: Summary of the results obtained by Jamroz *et al*

zinc having a density six times that of magnesium at equivalent temperatures.

Herman *et al* [4] made use of a heat pipe oven similar to the one used in this study. An external argon pressure of 100 Torr (=13.33 kPa) was applied which resulted in zinc vapour at 750 degrees Celsius and vapour pressure of 120 Torr (=15.996 kPa). Helium was added as buffer gas at a pressure of 90 Torr (=11.997 kPa). Jamroz *et al* [14] used a different heat pipe arrangement. The zinc was confined in a 35 cm long high temperature cell. Operating characteristics were: zinc vapour pressure of 50 Torr (= 6.650 kPa) and helium as buffer gas also at 50 Torr. No phase matching data was reported by Jamroz *et al* [14] and Herman *et al* [4].

Magnesium vapour is another suitable nonlinear material. By using the $3s4s^1S_0$ state (459.7 nm) and the $3s3d^1D_2$ state (431 nm) it is possible to tune over the range 174 - 140 nm [15]. Phase matching with krypton gas is possible and the ratio for perfect phase matching is 12.7 as determined by Junginger *et al* [16]. McKee *et al* [17] reported the generation of tuneable VUV radiation from 121 - 129 nm in magnesium vapour by using the $3s5s^1S_0$ state though reported intensities were smaller than those using the $3s4s^1S_0$ state and the $3s3d^1D_2$ state. Again phase matching with krypton gas was achieved.

The $5s^1S_0$ level of zinc is suitable for third harmonic generation at a VUV wavelength of 119.3 nm. Phase matching requires that one of the two gases in the mixture exhibit negative dispersion and the other positive dispersion. From the results of [4, 18, 19, 17] it is expected that phase matching with krypton and helium will not be possible at 119.3 nm due to the positive dispersion in this wavelength regime of both the respective buffer gases and the zinc vapour. For sum frequency generation at wavelengths above 120.3 nm it is expected that the addition of krypton gas could yield an increase in VUV generation due to the phase matching condition. More details are provided on the topic of phase matching in chapter 4.

2.7 The Heat Pipe and its Application to Spectroscopy

In section 2.5 the concept of phase matching was discussed. It was shown that phase matching plays an important role in the efficient generation of the third harmonic. It was also illustrated that phase matching can be achieved in practice by making use of a two component gaseous system. In the present study a two component gaseous mixture consisting of zinc vapour and helium gas was created inside a crossed heat pipe oven. For efficient generation of the third harmonic the zinc vapour and helium gas mixture needs to satisfy certain requirements. These include

1. A large zinc vapour density.
2. The temperature must be stable in time and constant to within a degree Celsius over a path length of roughly 7 cm.
3. The zinc and helium mixture needs to be homogeneous and stable.
4. The partial pressures of the zinc and helium gas need to be independently adjustable.

In point 1 above the large zinc vapour density is needed to enhance the value of $\chi^{(3)}$ which is directly proportional to the atomic density to be able to generate enough third harmonic radiation to be of any use. Point 4 is necessary to be able to achieve phase matching.

2.7.1 Brief History of the Heat Pipe

The heat pipe was first patented in the United States in 1944 as a solution to a refrigeration problem. Further development only began roughly twenty years after its invention. The development was pioneered by Grover *et al* [20] who coined the term heat pipe. As an engineering device it found a variety of applications in the aerospace industry, terrestrial fields and the cooling of electronics because of its ability to work without gravity and the high heat fluxes obtainable [21]. A few years after Grover *et al*'s [20] initial experiments Vidal

et al [22] took its development further and used it as a device to generate a well defined metal vapour column for spectroscopic measurements. They coined the term heat pipe oven to distinguish between the closed heat pipe used as an engineering device and the device they had developed for use as a spectroscopic instrument. Vidal *et al* [22] showed that heat pipe ovens facilitated the preparation of homogeneous metal vapour columns while avoiding contamination of the windows by the vapour.

2.7.2 Description of the Heat Pipe.

As an engineering structure the heat pipe consists of a closed pipe containing a working material and a wick structure fitted to the inside walls. If one end of the pipe is heated, the working material is boiled at the heated end of the pipe until it evaporates, it then travels as a vapour to the cool end where it condenses. Thus heat is transferred to the condensing end due to the latent heat of vapourization. The liquid formed at the condensing end returns to the boiling end through capillary action in the wick structure and gravity. Grover *et al* [20] also showed that the heat pipe can work without gravity. These principles are illustrated in figure 2.8. After some time a dynamic phase equilibrium is created. Evaporation and condensation are separated in space but take place at the same temperature and pressure. The temperature difference between the evaporation region and the condensation region is very small. Because of the large amount of heat transferred from the heated section to the cool section under such a low thermal gradient the heat pipe has a very large thermal conductivity. In initial experiments water was used as the working material in a porous Alundum tube serving as wick inserted into a tight fitting Pyrex tube [20].

The modified heat pipe oven constructed by Vidal *et al* [22] consists of a tube where the two ends are closed by a demountable unit which connects the tube to a vacuum chamber system and holds the windows in place this is shown in figure 2.9. The middle section of the tube contains a wick made from wire mesh. The central section of the tube is heated by an induction chamber. The tube is filled with an inert gas to a certain pressure. Once enough energy has been supplied to the system the working material will evaporate until the vapour pressure is equal to the inert gas pressure. Due to a slight pressure difference between the heated section and the unheated section on both sides the vapour

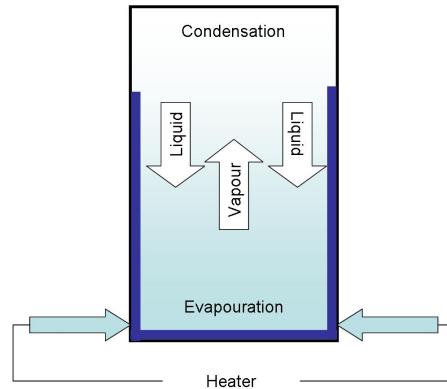


Figure 2.8: A Schematic illustration of the principle of the heat pipe.

diffuses into the unheated sections of the pipe where it condenses and returns to the middle portion of the tube through the wick by a capillary action. An equilibrium will be reached where the central section of the tube is filled with the working material as a vapour at a pressure equal to that of the inert gas. The temperature can be accurately determined from the vapour pressure curve of the working material.

2.7.3 Properties of the Heat Pipe Oven

There are several important properties of the heat pipe oven that bear mention:

1. The cold inert gas confines the vapour and alleviates the problem of metal vapour depositions on the windows.
2. The metal vapour is very clean. The constant evaporation and condensation purifies the vapour after some time. A molecular pumping action by the flowing vapour repels the buffer gas and any other impurities.
3. The heat pipe oven can be operated continuously under extremely well known conditions because the temperature difference over the length of the vapour column is less than one degree Celsius.

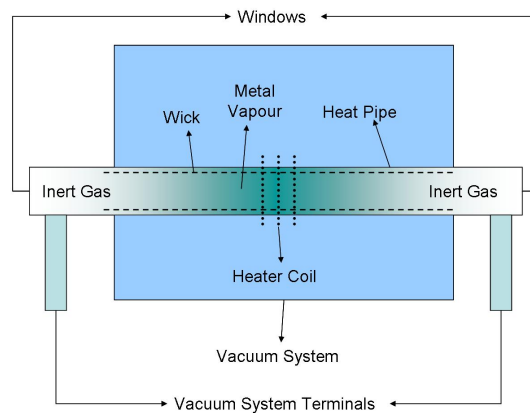


Figure 2.9: Illustration of the heat pipe oven developed by Vidal *et al* [22]

4. The pressure can be determined to a high degree of accuracy from the inert gas pressure. This determines the temperature through the vapour pressure curve.
5. The input power only determines the length of the vapour column and does not affect the temperature. An increase in the heating power results in the rate of evaporation increasing over the rate of condensation. The net effect is that the vapour column expands until heat losses over the larger outer surface balance the additional heating power.

It is possible to generate a stable homogeneous column of metal vapour constant to within a degree Celsius over a path length of a several centimeters or longer with the heat pipe.

2.7.4 The Crossed Heat Pipe Oven

The crossed heat pipe oven is used in the present study due to the need for metal vapour and inert gas mixtures with independently adjustable partial pressures. The design takes the form of a cross where the horizontal and vertical parts of the cross are two independent pipes as illustrated in figure 2.10. The vertical pipe acts as an isothermal oven for the section of the horizontal pipe that is

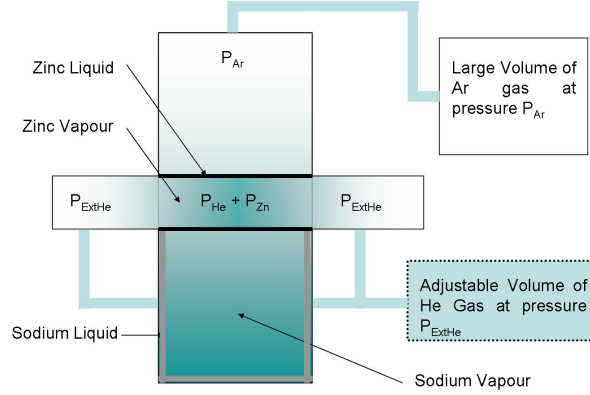


Figure 2.10: Illustration of the Crossed Heat Pipe Oven

enclosed by the vertical pipe. The vertical pipe functions as described in section 2.7.2, has sodium as working material and is maintained at a constant external argon pressure P_{Ar} . The horizontal pipe contains the components of the desired vapour-gas mixture, for example zinc and an inert buffer gas, in this case helium at pressure P_{ExtHe} . Sodium is chosen as working material in the vertical pipe because it has a higher vapour pressure than zinc at the same temperature and this results in stable operation. Argon was used because it is readily available and inexpensive. Zinc and helium are chosen for their optical properties.

The external argon pressure determines the temperature of the sodium and because of the thermal contact between the pipes the central portion of the horizontal pipe is maintained at this temperature. This temperature determines the partial vapour pressure of the zinc: $P_z(t)$. The external helium pressure P_{ExtHe} is chosen higher than $P_z(t)$ so that a homogeneous mixture of zinc and helium develops in the central portion of the horizontal pipe. The partial helium pressure is equal to the difference between the external helium pressure and the zinc vapour pressure

$$P_{He} = P_{ExtHe} - P_z(t) \quad (2.90)$$

The zinc vapour pressure is adjusted by changing the external argon pressure and the helium partial pressure is adjusted by changing the external helium pressure. At the edge of the mixture of zinc and helium the temperature and

zinc pressure decrease gradually resulting in an uncertainty in the density profile of the medium in these transition zones. Fluctuations in the heating power only affect the length of the sodium vapour column in the vertical heat pipe. As long as the vapour column extends past the central portion of the horizontal pipe the zinc and helium mixture is not affected. Generally heat pipe ovens have a certain warm up time which can be in the region of 3 hours, the crossed oven reduces the warm up time because a stable mixture of zinc and helium is created before the sodium vapour has reached its equilibrium position. The buffer gas confines the vapour column and stops the zinc vapour from condensing on the windows.

2.8 VUV Spectroscopy of Carbon Monoxide

2.8.1 Introduction to CO

Carbon monoxide is a colourless, odourless gas that consists of one carbon atom covalently bonded to an oxygen atom. It is an extremely stable molecule with a disassociation energy of around 9 eV [23] and a bond length of 0.1128 nm [24]. Carbon monoxide readily forms bonds to many transition metal centres. This is due to a low lying antibonding orbital concentrated on the C end to accept electrons from a filled d orbital of the metal. This explains its toxicity since CO will compete with O_2 for the iron centres of the hemoglobin in blood [25]. It is abundant in outer space and its absorption bands can be used to measure the density and heliocentric velocities of interstellar molecular clouds [5], [26]. This is the primary reason for the continued spectroscopic studies of the molecule: many rovibronic transitions have been calculated but laboratory wavelengths for these transitions have not been measured, particularly for the intersystem bands that are used to measure the density of interstellar molecular clouds in view of their low oscillator strengths [5].

2.8.2 Rovibronic Spectra

One of the applications of a tuneable laser source in the VUV is spectroscopy. An existing heat pipe oven using magnesium as nonlinear medium is currently in operation at the laboratory in Stellenbosch. This source has been used to measure rovibronic transitions in carbon monoxide. The setup is discussed in

more detail in section 3.2.1. There are three contributions to the total energy of the carbon monoxide molecule, these are electronic, vibrational and rotational:

$$E_{total} = E_{el} + E_{vib} + E_{rot} \quad (2.91)$$

When the molecule is excited to a new state the three different contributions to the energy change. The change in electronic energy results in a change in the angular momentum quantum number of the molecule. The vibrational state changes resulting in a change in the vibrational quantum number. Excitations to new electronic and vibrational states are known as vibronic bands. Within these vibronic bands lie the rotational transitions of the molecule. The allowed rovibronic transitions are governed by quantum mechanical selection rules. The rotational quantum number J may change by ± 1 or 0. This results in a three fold rotational structure known as the three branches: $\Delta J = 1$ corresponds to the R-branch, $\Delta J = -1$ corresponds to the P-branch and $\Delta J = 0$ corresponds to the Q-branch as indicated in figure 2.11. The rotational energy levels of the

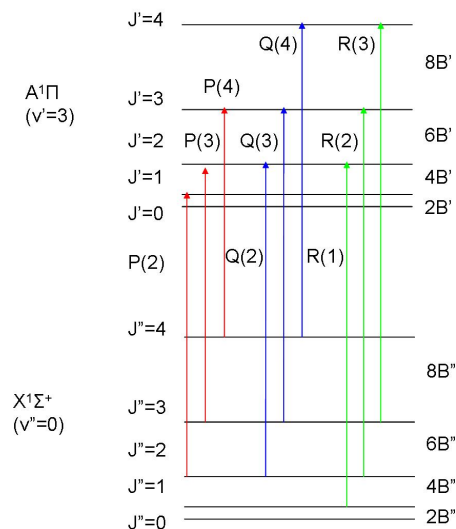


Figure 2.11: Rovibronic structure of a diatomic molecule.

molecule are spaced by multiples of the rotational constant

$$B = \frac{\hbar^2}{2I}, \quad (2.92)$$

where I denotes the moment of inertia of the molecule. From the rovibronic spectra it is possible to determine B thereby yielding some basic structural information of the molecule. The rotational constants are calculated by evaluating term differences. For every line in the P-branch, there is a corresponding line in the R-branch with the same upper state. For example R(3) and P(5) share the upper level with $J' = 4$. The wave number difference between these two lines is equal to the energy difference between the lower two states, that is between two rotational levels in the lower band. This wave number difference is given by

$$R(J-1) - P(J+1) = F_v''(J+1) - F_v''(J-1) = \Delta_v F''(J) \quad (2.93)$$

It is also possible to find a P and an R transition with a common lower state. By subtracting their term values the energy difference between the two upper states is obtained. This wave number difference is given by

$$R(J) - P(J) = F_v'(J+1) - F_v'(J-1) = \Delta_v F'(J) \quad (2.94)$$

These combination differences form a linear function of the rotational quantum number J given by

$$\Delta_v F'(J) = 4B_{v'}(J + \frac{1}{2}) \quad (2.95)$$

$$\Delta_v F''(J) = 4B_{v''}(J + \frac{1}{2}) \quad (2.96)$$

For a full treatment of the band spectra of diatomic molecules see [23]. Due to the sensitivity of the LIF technique it is possible to detect the rovibronic transitions of the four different isotopes existing in the sample of CO used [27]. The abundances of the four isotopomers are given in table 2.2

Isotopomer	Abundance %
$^{12}\text{C}^{16}\text{O}$	98.65
$^{12}\text{C}^{17}\text{O}$	0.037
$^{13}\text{C}^{16}\text{O}$	1.11
$^{12}\text{C}^{18}\text{O}$	0.202

Table 2.2: The natural abundances of CO.

Figure 2.12 [28] shows the electronic energy levels of carbon monoxide. The rotational structure within the $A - X$ electronic transition are well documented [26]. There are three other electronic states that lie close to the $A^1\Pi$ state as indicated in figure 2.12. These are the $d^3\Delta$, $e^3\Sigma^+$ and the $a^3\Sigma'$ triplet states.

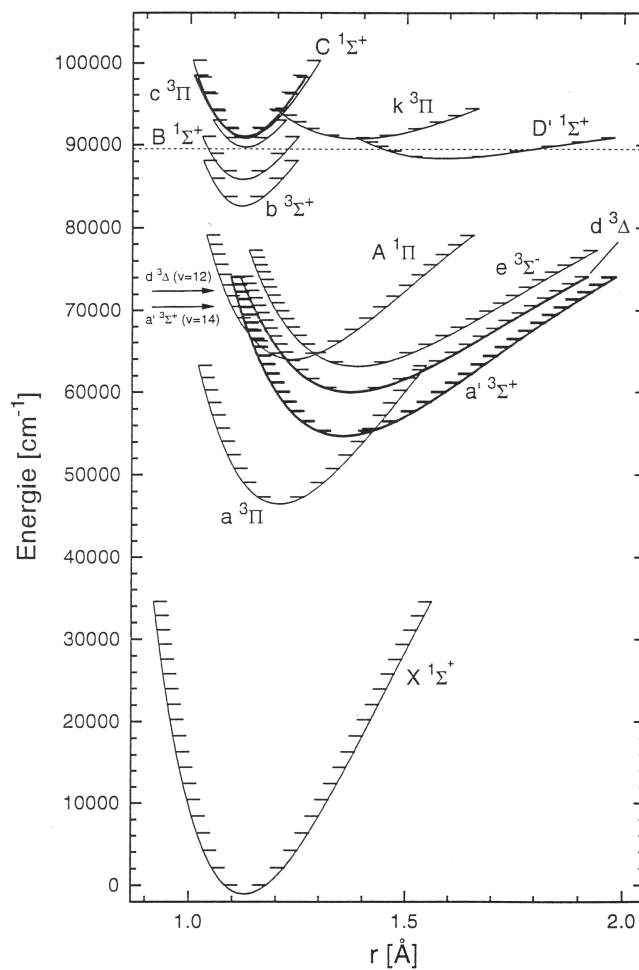


Figure 2.12: The potential energy curves for CO for various electronic configurations, the symbol $X^1\Sigma^+$ denoting the electronic ground state (singlet). The solid arrow illustrates a transition from the lowest vibrational level, following the Franck-Condon principle, and the dotted line below $90\,000\text{ cm}^{-1}$ denotes the dissociation limit .

Quantum mechanically the transitions from the ground state to any of these three states is forbidden [23]. This is relaxed due to spin orbit coupling and the transition probabilities are further enhanced due to the mixing of the triplet states with the $A^1\Pi$ singlet state [5]. Because of their small transition probabilities the triplet states have a much longer lifetime than the singlet states [29] Lifetimes of $4\mu\text{s}$ have been measured [30]. This characteristic can be used in the detection of the triplet states. Each rovibronic transition from the singlet ground state to one of the aforementioned triplet states is labelled according to its total electronic angular momentum. Due to spin orbit coupling the triplet state can have three different values of the total electronic angular momentum corresponding to the labels F1, F2 and F3 [31]. Calculated values for the wavelengths at which these transitions to the triplet states lie are in available [5], yet calibrated laboratory wavelengths for these transitions do not exist. The laser induced fluorescence (LIF) technique allows for the detection of these transitions to obtain accurately calibrated wavelengths.

The spectra are calibrated in one of two ways: by making use of a hollow cathode lamp or by making use of the well known transitions of the $A - X$ system. A small portion of the dye laser radiation is sent into a hollow cathode lamp (see section 4.1.1). Optogalvanic transitions of neon are well known and there are calibrated wavelengths from 272.4 nm up until close to the end of the visible portion of the electromagnetic spectrum at 730 nm [32]. Rotational transitions in the first four bands of the $A - X$ system are well known to a high degree of accuracy [26] and can be used to calibrate the spectra. This is particularly convenient when measuring the triplet states since they are often very close to the singlet transitions.

Chapter 3

Experimental Method

3.1 Setup for Four Wave Mixing in Zn Vapour

The experimental setup for the generation of third harmonic radiation is illustrated in figure 3.1. The excimer (Lambda Physik EMG 203) laser pumps the

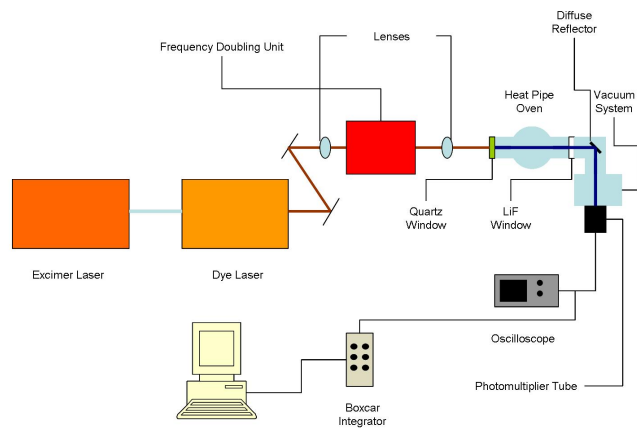


Figure 3.1: The setup for third harmonic generation in a crossed heat pipe oven with zinc as nonlinear material.

dye laser (Lambda Physik FL3002). The dye laser beam is reflected off two mirrors (Al on a glass substrate) and passes into the crossed heat pipe oven. The mirrors are needed to align the beam through the pipe. The nonlinear

process takes place inside the heat pipe and the resultant radiation passes into a vacuum chamber where it is detected by a photomultiplier tube. The vacuum chamber is evacuated by a Pfeiffer TPU 240 turbo molecular pump to a pressure of 10^{-6} mbar. The pressure is monitored by an Alcatel ACC 1009 cold cathode Pirani gauge. Two different photomultiplier tubes (PMT) were used in the detection of the generated VUV radiation. The first was the Hamamatsu R973 photomultiplier, which has a MgF_2 window, a detection range from 115 - 140 nm and can withstand a maximum photocathode voltage of 2 kV. The second photomultiplier used is the EMR 541J-08-18. It has a LiF window, a measuring range of 105 - 160 nm and can withstand a maximum photocathode voltage of 2.85 kV.

3.1.1 Lasers Optimisation and Calibration

The excimer laser used to pump the dye laser in the experiment was the Lamda Physik EMG 203. It is a high pressure XeCl pulsed gas laser producing light with wavelength 308 nm. The excimer laser is capable of producing pulses with energy of the order of 400 mJ with a pulse duration in the order of 20 ns. The repetition rate is adjustable from 1 Hz to 100 Hz.

The dye laser used in the experiment is the Lamda Physik FL3002. The tuneability of the dye laser allows for the generation of tuneable VUV radiation by four wave sum frequency mixing in the heat pipe which lends itself to spectroscopic applications (see section 3.2).

To achieve narrow bandwidth operation the dye lasers need to be aligned correctly. The dye lasers become misaligned very easily and constant maintenance is required to keep them running optimally. Tuning curves are taken regularly. They give information about the tuning range of the dye and is also a first indication as to whether the dye laser is lasing correctly. Tuning curves are taken by measuring the energy of the dye laser with the energy probe (laser probe RJP 735) while the wavelength of the laser is scanned manually in steps of 0.5 nm.

The dye lasers were calibrated using a see-through zirconium hollow cathode lamp. It is a spectroscopic device that is used as a spectral line source. It consists of a cathode made from the element that is to be investigated (in our case zirconium), an anode and a buffer gas all housed inside a glass tube. A plasma is created by applying a large voltage between the anode and cathode

thereby ionizing the buffer gas (usually a noble gas). Ions from the buffer gas are accelerated towards the cathode ejecting atoms from the cathode. The ejected atoms in turn are excited by collisions with other atoms in the plasma. When they decay back to their ground state they emit photons which can be detected and a spectrum can be determined. This primary function is not made use of, however the hollow cathode lamp displays another phenomenon known as the optogalvanic effect which is used to calibrate the dye lasers. The dye laser light is shone into the lamp and scanned over a region of the spectrum, when it is tuned to the correct wavelength it is possible to either photoionize the noble gas atoms inside the lamp (the lamp used contained neon) or excite them to levels from which they can easily be ionized by collisions. This increases the density of ions causing an increase in the current across the anode and cathode this results in a change in current which is measured. A boxcar integrator is then used to integrate the current signal. For a detailed discussion see [33]. In such a way a spectrum can be determined and matched against the known optogalvanic transitions of neon [32].

A Glan Taylor laser prism (GTLP) was used to investigate the polarization of the dye laser. The dye laser is vertically polarized [34]. The aim was to use the GTLP to investigate the degree of polarization of the dye laser, the losses due to insertion of the GTLP and to what extent the degree of polarization depends on the wavelength of the dye laser.

The GTLP is a polarizing beam splitter made from calcite. It consists of two prisms separated by a small air gap. It is transparent from 5000 nm in the infrared to 230 nm in the UV. It is a birefringent, uniaxial crystal. Due to its birefringence there are two specific polarization directions that experience different indices of refraction when passing through the crystal these are termed the e-ray and the o-ray for extraordinary and ordinary respectively. The o-ray experiences total internal reflection upon passing through the crystal. The e-ray passes straight through and the two calcite prisms are placed at a Brewster angle to minimise losses. By rotating the crystal around the azimuthal angle we are able to control how much of a component the incoming light has in each direction. The GTLP as a polarizer obeys Malus's law, that is the ratio of transmitted to incident intensity varies as $\cos^2\phi$. This was tested using a HeNe laser, a polarizer, the GTLP and a power meter.

The pulse shape of the dye laser was analysed with a Thor labs DET210 high speed silicon detector. A piece of paper with a pin hole was placed over the diode so as not to saturate the detector. The signal from the diode was sent

to an oscilloscope and the data was captured from there.

3.1.2 Second Harmonic Generation in a BBO Crystal

In chapter 2 frequency doubling and phase matching in a BBO crystal was discussed. Equation 2.85 gave the exact propagation direction for the light in the crystal to achieve perfect phase matching. In practice it is simply possible to rotate the crystal manually until the frequency doubled light is detected. To investigate the frequency doubling process in the case of doubling to 303 nm, a filter was used to block the fundamental after the crystal and then the 303 nm light was detected by looking at the fluorescence from a piece of white paper. The phase matching angle is critical and finer adjustments are made with a frequency doubling unit (Radiant Dyes Frequency Doubling Unit) illustrated in figure 3.2. The unit consists of two rotating stages that are coupled to one another. The first stage holds a compensator crystal which compensates for any deviation in the direction of the beam once it passes through the BBO crystal. The second stage contains the BBO crystal. A small amount of the frequency doubled light is sent onto a quadrant diode (UV-10BQ-4 from Laser Components GmbH). The quadrant diode consists of four photo diodes connected in pairs. Their signals are fed to the integrator inputs of the controller. In this way two rectangular surfaces or quadrants exist with a small gap between them. The photo diodes operate in difference mode so that a signal is generated when the two quadrants are illuminated differently. When the crystal is in position for maximum doubling efficiency the two quadrants are illuminated equally. If the wavelength of the laser changes by a small amount, the phase matching angle will change and the two quadrants will no longer be illuminated equally. The frequency doubling unit then rotates the crystal until the position for optimum doubling efficiency is found, i.e. when the quadrants are again illuminated equally. All of the actions are computer controlled. There is an option to manually control the frequency doubling unit. It is then possible to rotate the crystal in steps of 0.00015 degrees using the computer. The energy of the frequency doubled light was then measured with a wavelength independent RJP 735 pyroelectric energy meter. The phase matching data was recorded at low input energy so as to not damage the crystal. The crystal was rotated in steps of 0.0225 degrees using the computer controller and the energy of the output was recorded by the energy meter. The actual phase matching angle was not

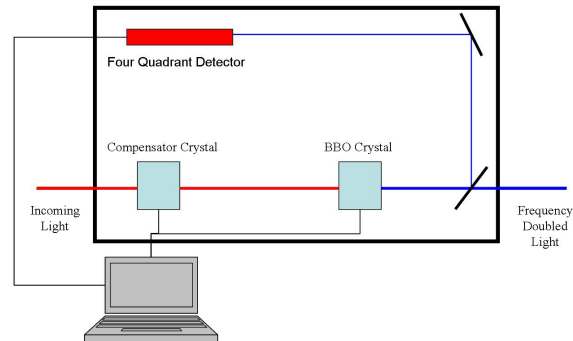


Figure 3.2: A depiction of the frequency doubling unit used in the experiment.

measured. The absolute angle is not known, only the change in angle as the crystal was rotated.

Three lenses were tested to focus the light onto the crystal so as to investigate the dependence of second harmonic generation on the intensity of the input beam. The three lenses used had focal lengths of 40 cm, 30 cm and 25 cm respectively. Initially the beam was focused roughly 2 cm from the crystal so as to avoid damaging the it. The energy of the second harmonic light was measured with the energy meter.

The phase matching angle of the crystal is dependent on the wavelength of the incident radiation. In order to investigate how critical this dependency is the crystal was phase matched for an incident wavelength of 606 nm, the wavelength was then changed in steps of 0.2 nm. The energy was measured by the energy probe.

3.1.3 Construction and Development of the Heat Pipe Oven

The three main steps in the construction process of the heat pipe oven are:

1. Mounting and insulation of the pipe.

2. Construction of the gas handling system to control the helium and argon pressures.
3. Loading working materials into the heat pipe and cleaning the system.
4. Construction of the vacuum chamber into which the VUV radiation propagates.

The heat pipe is heated via a normal oven element and needs to be insulated so as to reduce warm up times and maintain a stable temperature. The element is connected to a variable transformer so that the voltage applied across the element can be changed from 0 - 220 V. The current supplied was 4 A so as to not exceed the limit of 1800 W of power that can be supplied to the heating element. The temperature of the heat pipe is controlled by changing the pressure of an external volume of argon gas connected to the heat pipe. A system was constructed using quarter inch copper piping and a series of valves to connect the external volume to a pump and to the vertical portion of the heat pipe. The argon pressure was monitored with an MKS 622A pressure transducer. Inside the vertical pipe at the heated end is a wick structure made from stainless steel mesh. The wick ensures an even spread of sodium in the heating zone. If there is not enough sodium or an uneven distribution thereof there is a possibility of so called "hot spots" forming. "Hot spots" may damage the heat pipe wall due to overheating and may disrupt the stable operation of the heat pipe. A spiral plate is inserted inside the vertical pipe and rests on top of the horizontal pipe. It prevents the sodium liquid from dripping onto the horizontal pipe thereby causing fluctuations in the temperature. Two small stainless steel clamps were welded to the vertical pipe at 7 cm and 18 cm above the horizontal pipe. Two K-type thermocouples are inserted into the clamps. They give an indication of how high up the pipe the vapour column has reached. Due to the poor heat conductivity of the stainless steel the thermocouples cannot give an absolute measure of the temperature inside the heat pipe. The absolute temperature, which can be read from the sodium vapour pressure curve is determined by the argon pressure. The heating power must be adjusted so that the vapour column extends past the lower thermocouple but does not exceed the height of the upper thermocouple. Stable operation of the pipe is reached when the readout of the lower thermocouple does not vary with time.

The horizontal pipe houses the mixture of zinc vapour and helium gas. It is enclosed by a quartz window on one end and a lithium fluoride window on the other end. The vertical pipe acts as an isothermal oven for the horizontal pipe. The mixture is heated up to a temperature of above 750 degrees Celsius, determined by the vapour pressure curve of sodium. This then determines the partial pressure of the zinc vapour in the mixture. The helium gas has a dual purpose: it is needed to ensure the condition of phase matching as well as confine the zinc vapour column to the central portion of the pipe thereby stopping it from condensing on the windows of the system. There is a small transition zone where the zinc vapour meets the helium gas; the temperature is not well known at this point. The insulation around the horizontal pipe is cut away so as to keep the temperature gradient at the transition zones as steep as possible. A wick structure made of stainless steel mesh is inserted inside the horizontal pipe. It serves to remove liquid zinc from the outer region back to the middle region where evaporation can take place. It is possible for a small portion of the zinc vapour to reach the cooler portion of the horizontal pipe thereby forming crystals. These crystals can be removed by heating that section of the pipe with a small handheld burner.

The pressure of the helium gas supplied to the horizontal portion of the pipe needs to be adjustable in order to achieve phase matching. An adjustable, volume known as a bellows, constructed in the workshop at Stellenbosch is connected so as to be able to vary the pressure. Sodium has a melting point of just above 97 degrees Celsius and is kept in paraffin to prevent it from reacting with water vapour in the air. Consequently upon inserting the sodium into the heat pipe, a fair quantity of paraffin and other impurities make their way into the pipe. The heat pipe must then be filled with argon and heated to just above the melting point of sodium several times, each time evacuating the pipe once it has cooled, so as to remove the impurities. The vertical pipe is first loaded with sodium and argon. When the vertical pipe is operational the horizontal pipe is loaded with zinc and helium. Care was taken to ensure that the zinc metal was inserted as close to the centre of the pipe as possible.

The vacuum chamber into which the VUV radiation propagates was mounted onto a movable trolley and connected to a turbo pump. This was then connected to the heat pipe oven by a standard KF-40 flange.

3.1.4 Four Wave Mixing in Zinc Vapour

3.1.4.1 Setup for Resonant Enhancement using the $5s^1S_0$ Level

The setup for resonant enhancement using the $5s^1S_0$ level and the subsequent generation of VUV radiation at 119.3 nm is illustrated in figure 3.1. The frequency doubling unit was removed for this experiment. Resonant enhancement using the $5s^1S_0$ level required pumping of DMQ dye to produce light of wavelength 358 nm. The dye laser was calibrated for this region using the hollow cathode lamp and the wavelength region from 357.8 - 359.9 nm was scanned. The exact wavelength for the two photon resonance is not known. Herman *et al* [4] specify it as 358.5 nm where as Jamroz *et al* [14] specify it to be at 358.8 nm. The energy of the light entering the heat pipe was in the order of 0.6 mJ. Three different lenses were used to focus the radiation into the middle of the heat pipe. First a CaF lens with focal length 400 mm was used and then a quartz lens with focal length 300 mm and finally a quartz lens with focal length 800 mm.

Two photomultiplier tubes were used in the detection of the VUV radiation. The first was a Hamamatsu R973 photomultiplier it is a solar blind photomultiplier tube with a measuring range from 115 - 200 nm and a peak at 140 nm. Its photo cathode is made from Cs-I. The second photomultiplier used was the EMR 541J-08-18. Also a solar blind photomultiplier with a photo cathode made from KBr with a measuring range from 105 - 150 nm. The heat pipe was operated with an external He pressure of between 80 and 220 Torr. The Ar pressure was kept constant at 100 Torr.

3.1.4.2 Setup for Resonant Enhancement using the $4s6s^1S$ Level

The $4s6s^1S$ level required frequency doubling of the dye laser radiation in order to obtain $\lambda_2 = 302.8 \text{ nm}$. The setup in figure 3.1 was changed only slightly by the inclusion of the frequency doubling unit between the dye laser and the heat pipe. Rhodamine B dye was used, it has a tuning range of 588 - 640 nm. The wavelength was set to 605.6 nm and sent into the BBO crystal in the frequency doubling unit where frequency doubling takes place. Only the 400 mm CaF lens was used to focus the radiation into the heat pipe. This was due to the insertion of the frequency doubling unit. The frequency doubling unit was placed relatively close to the entrance to the heat pipe so as to minimise the path length over which the frequency doubled beam travels thereby minimising

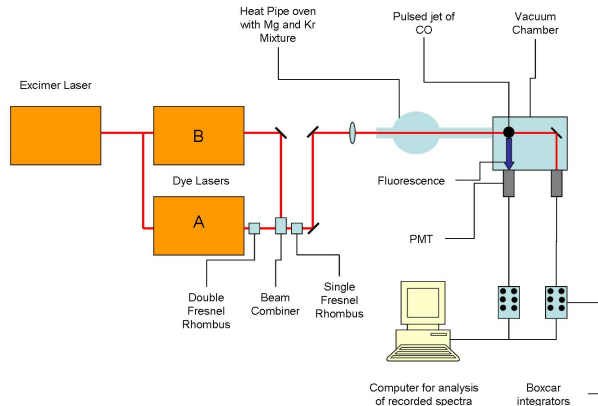


Figure 3.3: The setup used for VUV spectroscopy of CO.

losses. The 300 mm quartz lens was used to focus the dye laser radiation into the BBO crystal. The heat pipe was operated at a fixed helium pressure of 90 Torr. The argon pressure was kept constant at 100 Torr.

3.2 Setup for VUV Spectroscopy of CO

The current setup at Stellenbosch University as illustrated in figure 3.3 employs a crossed heat pipe oven to generate a homogeneous mixture of magnesium vapour and krypton gas. The setup and its uses are described in detail by Steinmann [33] and only the most important aspects are discussed here. In this thesis the crossed magnesium heat pipe was used to measure a number of rovibronic transitions of carbon monoxide thereby demonstrating the uses of a tuneable source of VUV radiation.

3.2.1 Setup for Sum Frequency Generation in a Magnesium Vapour

At approximately 800 degrees Celsius a homogeneous column of magnesium vapour and krypton gas is generated suitable for the efficient generation of sum frequency radiation. The crossed heat pipe oven again uses sodium as

working material in the vertical pipe and the temperature is again controlled by an external argon pressure. Pressures between 24 and 25 kPa produce a temperature of 680 degrees Celsius. Typical warm up times are in the region of 2 hours and the heat pipe is able to maintain stable operating conditions well over 9 hours. The buffer gas used in the system is krypton, again chosen for its optical properties. Typical pressures used are in the range of between 20 and 40 kPa. The krypton pressure can be adjusted by a bellows connected to the system. This is to ensure that the phase matching condition is met.

One of the dye lasers is set on a fixed wavelength to coincide with the two-photon resonance of magnesium at 430.88 nm. The other dye laser can be tuned across the available bandwidth of the dye thus providing tuneable radiation in the VUV. Typical dye laser pulse energies are in the region of 1 - 1.5 mJ measured after the polarizing beam combiner. The dye laser set to the fixed frequency ω_1 (henceforth known as dye laser A) is sent through a double Fresnel rhombus so as to change its polarization from vertical to horizontal. This allows the beam to pass straight through the polarizing beam combiner. The second dye laser (henceforth known as dye laser B) at frequency ω_2 is vertically polarized and sent onto the polarizing beam combiner by a mirror. Upon entering the beam combiner dye laser B is totally internally reflected so as to be in the same direction as dye laser A. The dye lasers are now colinear. Once colinear the dye lasers pass through a single Fresnel Rhombus so that the beams become circularly polarized in opposite directions as discussed in section 2.4.4. The two colinear dye laser beams pass into the heat pipe after reflections off two mirrors. The mirrors are needed for alignment through the pipe. Once in the heat pipe they undergo four wave sum mixing to produce tuneable radiation in the VUV. The VUV radiation passes to a vacuum chamber evacuated by a Pfeiffer TPH 200 Turbo molecular pump where it is detected by a Hamamatsu R973 photomultiplier tube described in section 3.1.4.

3.2.2 LIF Spectroscopy of CO

The tuneable narrow bandwidth VUV radiation produced in the Mg/Kr crossed heat pipe oven is well suited for generating LIF excitation spectra of CO. Once in the vacuum chamber the VUV radiation interacts with a pulsed supersonic jet of CO. The jet of CO is supersonically expanded to cool the CO sample. Low sample temperature greatly simplifies the LIF spectra that are recorded [29].

The fluorescence generated when the VUV radiation is tuned to a rovibronic transition is detected by a Hamamatsu R973 photomultiplier tube. The signal is passed onto a boxcar integrator where it is integrated and then sent onto a computer for analysis. With the boxcar integrator it is possible to set over how much of the signal to integrate (Gate Width) and when the integration time begins (Gate Delay). It is also possible to set the time between the laser pulse and the gas pulse, this is known as the pulse delay.

3.2.2.1 Detection of Singlet-Singlet Transitions

The singlet-singlet transitions were measured with gate widths in the region of 10 ns and gate delays of 30 ns. The signals of the singlet-singlet transitions can be optimised by changing the conditions in the supersonic jet. By adding argon to the mixture it is possible to further simplify the spectra by forcing more of the CO into the lowest vibrational state. Upon colliding with another atom or molecule the argon converts some energy into kinetic energy. Thus inelastic collisions between argon atoms and CO molecules result in the conversion of some rotational and vibrational energy into kinetic energy, thereby increasing the population of the lowest levels [29]. The spectra were recorded at either one bar pure CO or a mixture of one bar CO and 3 bar Ar.

3.2.2.2 Detection of Singlet-Triplet Transitions

A pressure of 1 bar of CO in the jet was used for the detection of the so called “forbidden” transitions of CO. The signals of these transitions can be extremely weak, the operating voltage on the photomultiplier was turned to a maximum of 2kV. Typically for the measurement of the forbidden transitions the gate width was set to between 200 and 300 ns and the gate delay between 100 and 200 ns. This enables one to suppress the detection of the stronger singlet-singlet transitions. The forbidden transitions have a much longer lifetime as discussed in section 2.8 and thus their fluorescence is still detected at these delayed integration times. The delay between the laser pulse and the CO gas pulse was set to between 500 and 650 μ s. Each point on the spectra is averaged over ten shots from the laser.

Chapter 4

Experimental Results and Discussion

4.1 Dye Laser Characterisation

4.1.1 Dye Laser Calibration

A typical optogalvanic calibration spectrum measured using a zirconium hollow cathode lamp is shown in figure 4.1. The lines are mostly lines of neon that is the buffer gas in the lamp. The wavelengths of the spectral lines are calibrated by comparison with an optogalvanic atlas [32]. Only those lines known to seven significant figures are used. The calibration function is calculated by making a least squares fit as illustrated in figure 4.2. Usually a linear fit is fitted due to the relatively small region over which the scan is taken. The energy of the dye laser has to be monitored daily and tuning curves need to be taken regularly. Figure 4.3 shows a typical tuning curve of a dye laser containing Rhodamine B, which can be compared to the tuning curve of the manufacturers of the dye in this case Lamda Physik. The tuning curve provides one with an early indication as to whether the dye laser is lasing correctly.

4.1.2 Limitations of the Calibration Technique

There are two limiting factors with this calibration technique. Firstly many of the transitions in the optogalvanic spectrum of neon are only known to six

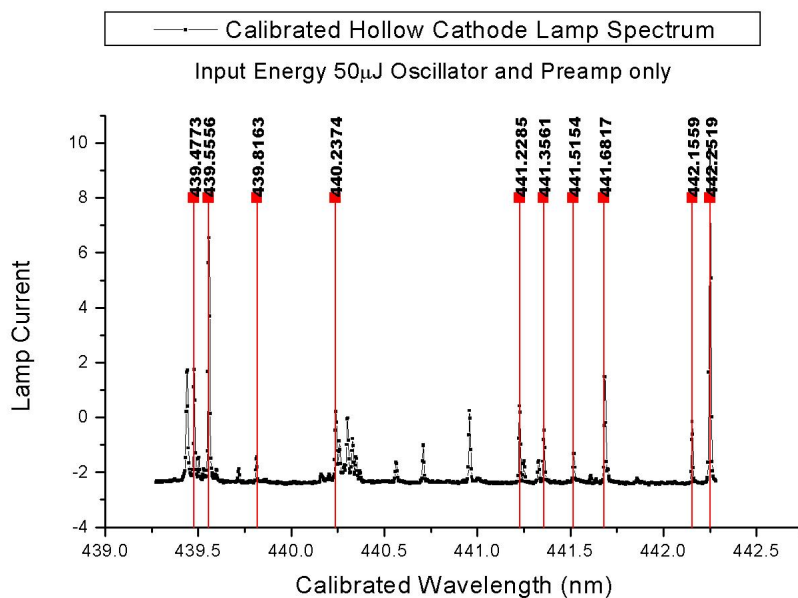


Figure 4.1: A calibrated optogalvanic spectrum of Neon. This was taken without the main amplification stage of the dye laser.

significant figures. The main use of the VUV source will be for spectroscopy of CO and other diatomic molecules. The present standard is set by measuring rovibronic transitions accurate to at least seven significant figures which requires that the wavelength of the dye laser be known accurately to seven significant figures. Because there are so many transitions of the molecule that can become excited inside the plasma it is impractical to compare the optogalvanic transitions to absorption spectra of neon which are well known and accurate seven significant figures.

The second limitation is power broadening. By increasing the intensity of the laser entering the lamp it is possible to increase the signal strength, at some point the spectra will become power broadened and closely spaced lines will become unresolvable. However this can be overcome by limiting the intensity of the dye laser light by use of a GTLP or reflecting some of the radiation off a glass plate into the lamp.

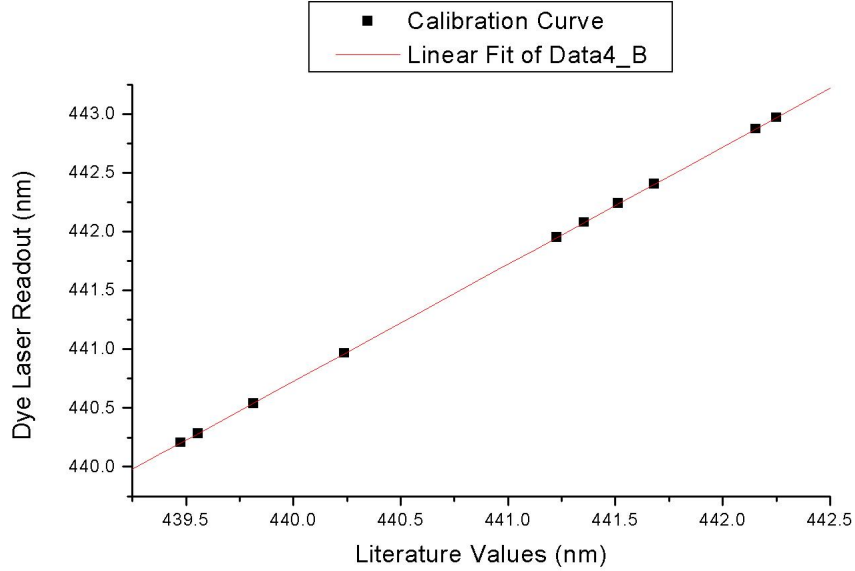


Figure 4.2: The calibration curve used in the calibration of the spectrum in figure 4.1. A linear fit was applied and the calibration equation was $y = 2.0048 + 0.9970 \times x$.

4.1.3 Polarization of the Dye Laser

In order to discover to what extent the dye laser is vertically polarized a Glan Taylor laser prism (GTLP) was used. Initial experiments with the GTLP were conducted with a HeNe laser, polarized by a linear polarizer, in order to verify that the GTLP as a polarizer obeys Malus's law. It was found that by rotating the GTLP by hand it was possible to reduce the transmitted power of the HeNe laser to 0.01 mW which is 1% of its total power. The results of the experiment are shown in figure 4.5. The actual point for zero degrees was not known and so the rotation began at an arbitrary angle, this is the reason for the rotation beginning at (0,0) and not (0,1). The results thus show that the GTLP as a polarizer obeys Malus's law and the linear polarizer polarizes the beam 99%.

Using a similar technique the percentage polarization of the dye laser was investigated. The percentage polarization was defined as

$$\frac{\text{max intensity}}{\text{max intensity} + \text{min intensity}} \quad (4.1)$$

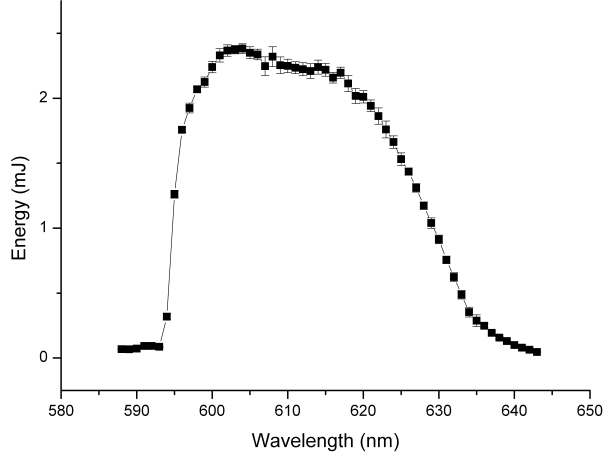


Figure 4.3: Tuning Curve of a dye laser operating with Rhodamine B dye

where the “max intensity” was the highest intensity obtained at a specific wavelength while rotating the GTLP and the “min intensity” was the minimum intensity measured when rotating the GTLP. Results are shown in figure 4.6 and indicate that at the peak of its tuning curve the dye laser is in the region of 85 - 90 percent polarized in the vertical direction. The losses due to the insertion of the GTLP were determined by calculating the percent transmission of the GTLP at the angle for maximum transmission.

$$1 - \frac{\text{max intensity}}{\text{intensity with no polarizer}} \quad (4.2)$$

It was found that losses around the peak of the dye are in the region of 20-30 percent as shown in figure 4.7 .

4.1.4 Pulse Shape of the Dye Laser

The pulse shape of the dye laser was measured and found to consist of two peaks. This is due to the many modes oscillating within the dye laser cavity. The peaks originate due to the beating caused by the different longitudinal modes oscillating within the cavity. From the measurement in figure 4.8 the pulse width was in the order of 20 ns with pulse energy in the order of 1.2 mJ.

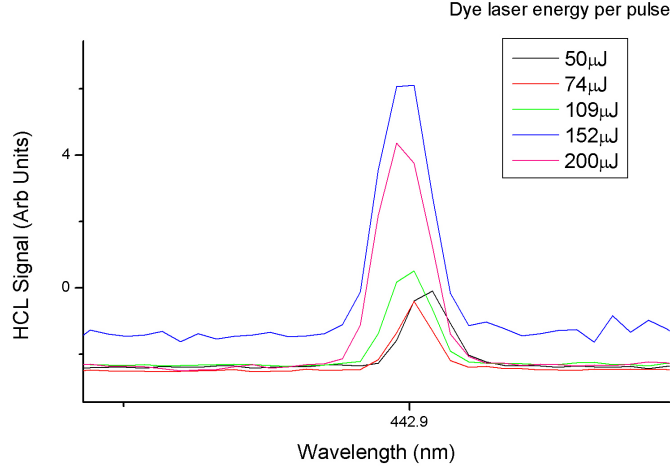


Figure 4.4: Illustration of the effect of power broadening.

The resultant peak power was therefore 60 kW. The power is comparable with the output powers achieved by Herman *et al* [4] who successfully achieved four wave sum mixing in a zinc vapour with similar dye lasers and powers in the region of 50 - 200 kW.

4.2 Characterisation of the Frequency Doubling Unit

The BBO crystal is efficient for UV generation from 205 to 310 nm with conversion efficiencies in the range of 10%. Conversion efficiencies of 36% have been achieved using a XeCl pumped dye laser with power of 150 kW [35]. The dye laser used in the experiments had roughly half of this peak power typically 60 kW therefore we expected efficiencies below this mark.

Two factors important for efficient generation of the second harmonic are phase matching and the input power per square centimeter.

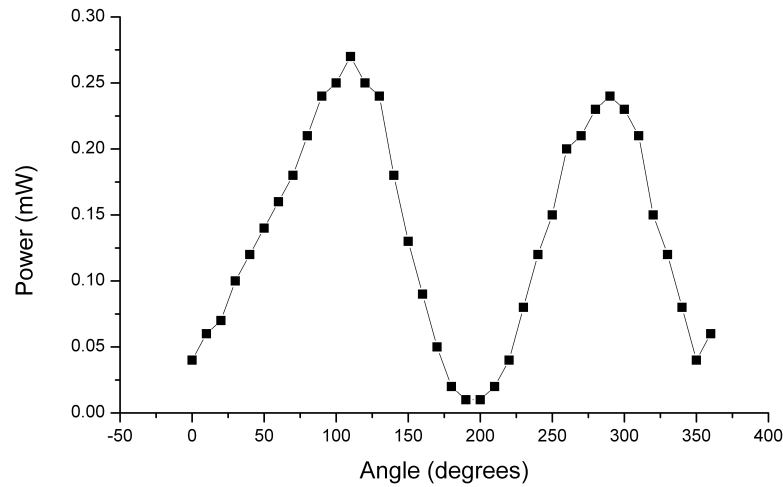


Figure 4.5: A graph of transmitted power of the polarised HeNe laser beam against the angle at which the GTLP was rotated.

4.2.1 Experiments with Rhodamine B Dye

Experiments were conducted with Rhodamine B dye which has its peak at 600 nm. The wavelength of the light was halved from 606 nm to 303 nm so as to be close to the two photon resonance of zinc at 302.8 nm [14].

4.2.1.1 Phase Matching

The result is shown in figure 4.9. The input intensity was in the order of 0.4 mJ and the focussing done with a lens of focal length 30 cm to avoid any damage of the crystal. It was not possible to measure any more peaks, at this input intensity, in the phase matching curve due to the signals being smaller than the threshold for detection by the energy probe. The angle for perfect phase matching actually occurs twice, one each side of the normal. The angle on the other side of the normal has oscillations to the left of the main peak.

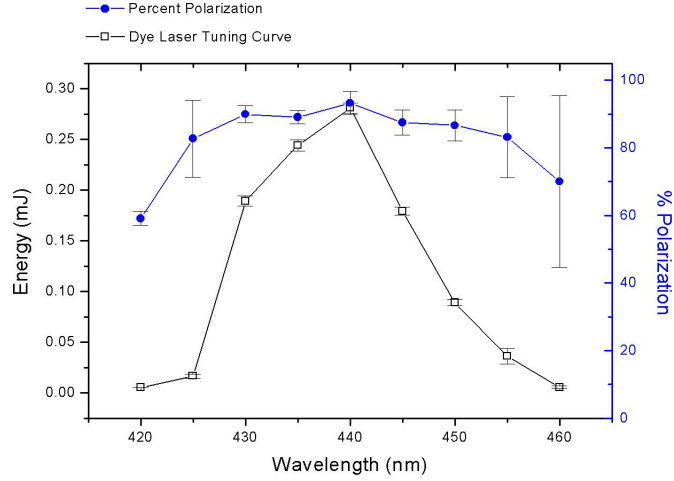


Figure 4.6: The percentage polarization of the dye laser plotted together with the tuning curve of the dye used in the experiment.

4.2.1.2 Experiments with Lenses

The second order nonlinear process goes with the square of the intensity and without focusing the light there was simply not enough intensity to achieve frequency doubling. The results are summarised in table 4.1. As can be seen

Focal Length (cm)	40	30	25
Output (303 nm) (μJ)	30	40	44
Efficiency (%)	2.30	3.07	3.38

Table 4.1: A tabulation of the results obtained for frequency doubled light using different lenses.

from the table the efficiency increases as the focus gets tighter. The damage threshold of the BBO crystal is $5 \frac{GW}{cm^2}$ for 10 ns pulses [8] and it was found that by focusing the beam in the middle of the crystal with the 30 cm lens we are close to this threshold. No further attempts were made to focus the beam tighter than this. Using the 30 cm focal length lens the focus was then shifted to the middle of the crystal. The input energy was attenuated with the Glan Taylor laser prism and the focus was shifted until maximum second harmonic energy was obtained. A maximum output of 0.135 mJ was achieved for an input of 0.968 mJ yielding an efficiency of 13.9%. This test was not conducted with

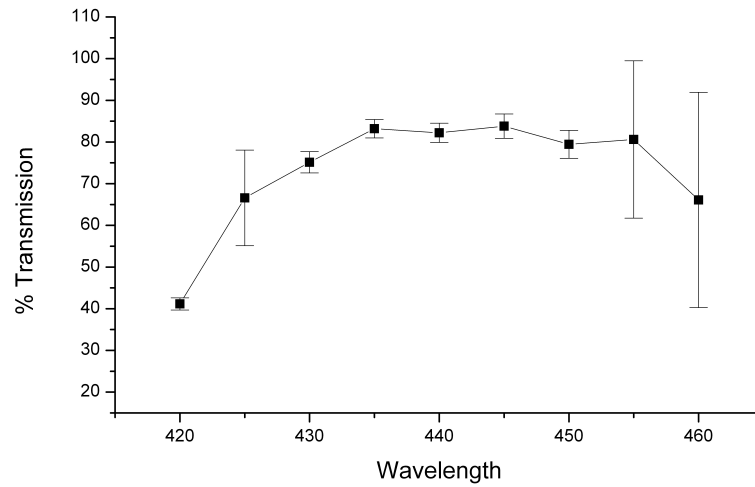


Figure 4.7: Figure showing the percent transmission of the dye laser through the GTLP. This gives an indication of the losses.

the lens of focal length 25 cm for fear of damaging the crystal.

4.2.1.3 The Dependence of the Phase Matching Angle on the Wavelength

As can be seen in figure 4.10 the wavelength can be tuned over a large region without adjusting the crystal angle to optimise phase matching before the efficiency of the nonlinear process starts to decrease. This is convenient when having to scan the wavelength while searching for the two photon resonance of the zinc vapour.

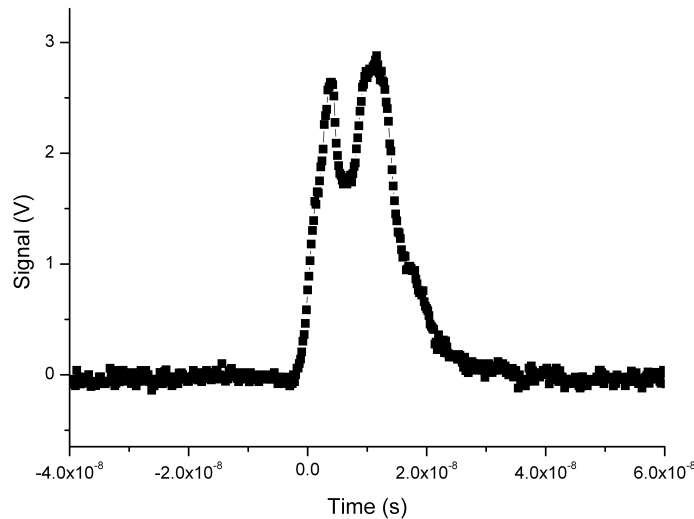


Figure 4.8: The pulse shape of the dye laser.

4.3 Experimental Results for Four Wave Mixing in a Metal Vapour

4.3.1 Experimental Results for Sum Frequency Generation in Mg Vapour

The setup for the generation of tuneable VUV radiation in a magnesium krypton vapour medium was optimised by adjusting the partial pressure ratio between the magnesium and krypton to achieve phase matching, by adjusting the overlap between the two beams and focusing of the beams into the medium.

25 kPa of Ar resulted in a temperature of 680 degrees Celsius. To this, between 32 and 35 kPa of Kr was added to achieve optimal phase matching. This is illustrated by the phase matching curve in figure 4.11 . The two photon resonance of Mg was found to be at 430.8771 nm as illustrated in figure 4.12. The resonance has a FWHM of 0.0129 nm. The dye laser providing the tuneable photon in the sum frequency process had a tuning range of 40 nm from 420 to 460 nm this allowed for tuning from 142.3 to 146.7 nm. The overlap between the two beams was critical for efficient sum frequency generation. The overlap was adjusted by changing the position of the beam combining crystal. The crystal

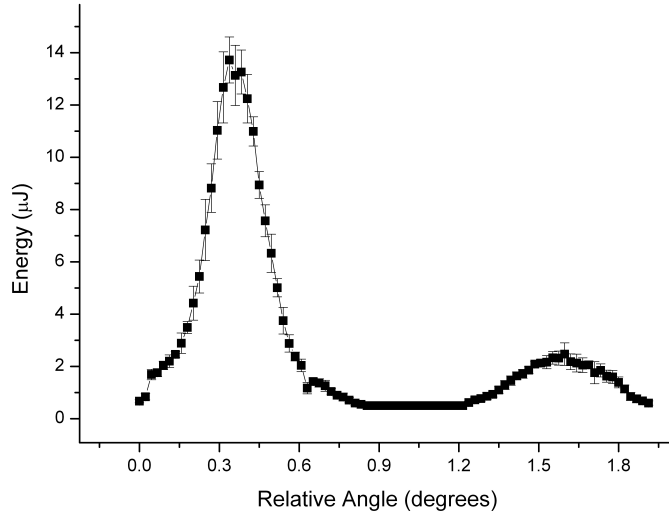


Figure 4.9: Phase matching curve taken for a BBO crystal. The BBO crystal is phase matched by angle tuning.

is mounted on a stage that provides for fine adjustment in the horizontal and vertical directions. The beams were focused using an 80 cm focal length lens. The focus was not too tight so as to make use of the whole vapour column in the nonlinear process. The intensities of the dye lasers depend on several factors as illustrated in section 4.1, when they are running optimally the combined beam intensity entering the heat pipe is in the order of 2.5 mJ. The voltage on the Hamamatsu photomultiplier was set to 1.5 kV at these optimal conditions. The threshold input intensity for third harmonic generation was found to be in the order of 0.1 mJ. Under these conditions the voltage on the Hamamatsu photomultiplier was set to a maximum of 2 kV.

4.3.2 Experimental Results for Third Harmonic Generation and Sum Frequency Generation in Zn Vapour

4.3.2.1 Resonant Enhancement using the $5s^1S_0$ Level

Scans taken with the Hamamatsu photomultiplier were inconclusive. It was discovered that although the photomultiplier is solar blind and is only supposed

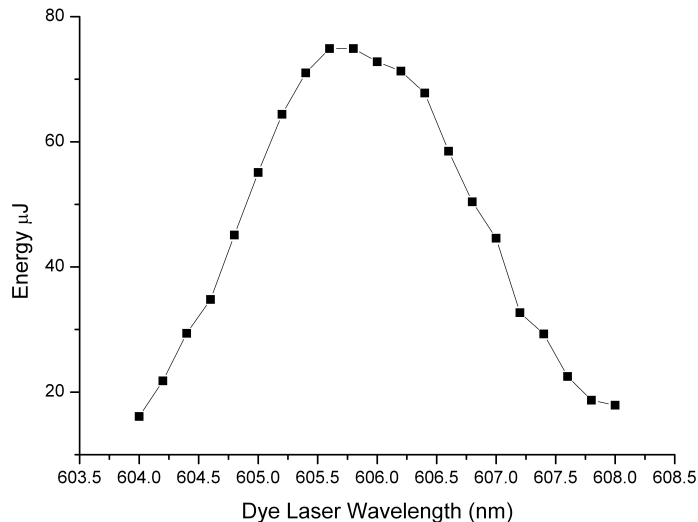


Figure 4.10: A graph depicting the wavelength tuneability of the BBO crystal. The crystal was phase matched for 606 nm.

to show a response between 115 and 140 nm it responded to the light from the dye laser at 358 nm. A diffuse reflector was introduced and the supply voltage to the photomultiplier was reduced from 2 kV down to 1.8 kV to avoid saturation of the background signal. The result is a measurement taken on a non-zero background. The window on the Hamamatsu photomultiplier is MgF_2 which transmits only 35% at 119 nm. At the exit side of the heat pipe is a LiF window which transmits 70% at this wavelength. Thus it is only possible to detect 24.5 % of the photons at 119 nm.

It was discovered that the EMR photomultiplier was also sensitive to the UV radiation from the dye laser at 358 nm. Supply voltages between 1 and 2 kV were used with the beam from the heat pipe falling directly onto the photomultiplier. A result was obtained using this configuration and focusing the incident beam with the 30 cm quartz lens into the heat pipe. Figure 4.13 shows the possible location of the two photon resonance of zinc. Unfortunately the circulator of the dye laser stopped working before the scan could finish. That is why the signal suddenly drops to zero after the peak. The centre of the peak sits at 357.7497 nm as indicated on the figure. There is thus a slight

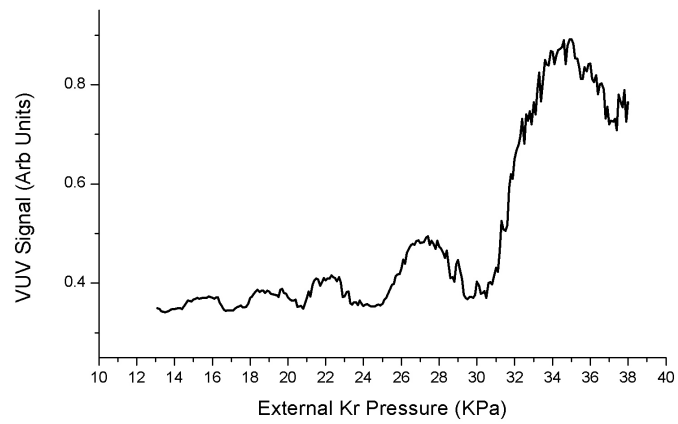


Figure 4.11: Phase matching curve of the Mg heat pipe oven.

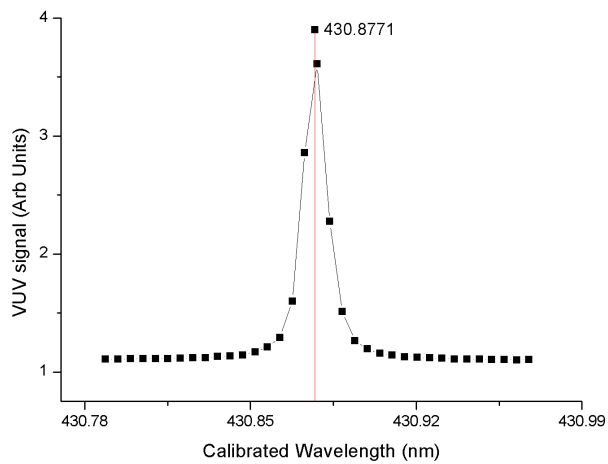


Figure 4.12: A scan of the resonance of magnesium.

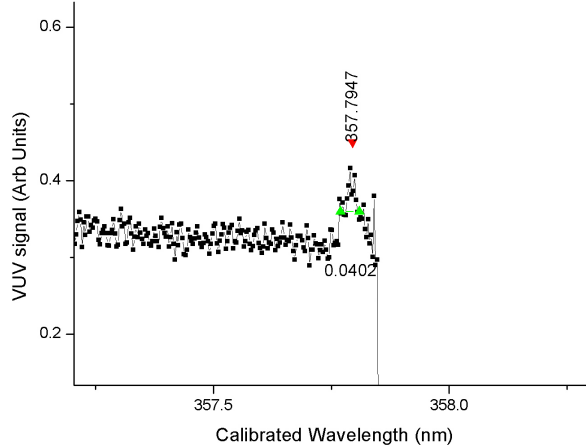


Figure 4.13: Graph indicating the position and FWHM of the two-photon resonance of zinc.

discrepancy with the values of Jamroz *et al* (358.5 nm)[19] and Herman *et al* (359 nm) [4]. The FWHM of the peak is in the order of 0.0402 nm as indicated in figure 4.13 . The signal is very small and the calculation of the FWHM is only a rough one but it appears that the width of the resonance is in the same order of magnitude as that measured with the magnesium heat pipe. The diffuse reflector was again introduced. The background signal then disappeared and the operating voltage on the EMR photomultiplier was increased to 2 kV. The experiments were repeated but were unsuccessful.

The incident power of the laser is relatively low and the conditions are not optimal: the third harmonic intensities are thus expected to be very small initially. The conditions cannot be optimised without first observing the signal. The detection of the third harmonic signal is made difficult by the large background due to the sensitivity of the photomultiplier for the incident light. This is most likely obscuring the small signal. It is also making it necessary to turn the supply voltage of the photomultiplier down therefore reducing sensitivity. The introduction of the diffuse reflector reduces the background signal but also reduces the amount of third harmonic incident on the photomultiplier. With the intensities being really low with the unoptimised system it is probably not possible to detect the signal using this configuration. The possible solutions are to increase the incident power or separate the incident and VUV beams in the

vacuum chamber. Increasing the power is not possible with the current experimental configuration. Separating the beams is a possibility, this could be done by introducing a LiF prism into the vacuum chamber.

4.3.2.2 Resonant Enhancement using the $4s6s\ ^1S$ Level

Resonant enhancement using the $4s6s\ ^1S$ level required frequency doubling of dye laser radiation at 605.6 nm in a BBO crystal to produce radiation at 302.8 nm. Third harmonic generation using this two photon resonance was not observable due to the LiF window cut off at 105 nm. The sum frequency of the fundamental light with the frequency doubled light $\omega_s = 2\omega + 2\omega + \omega$, where ω is the wavelength of the fundamental and 2ω is the frequency of the doubled light will yield VUV radiation of wavelength 121.12 nm that can be observed. The experiments were conducted with the Hamamatsu photomultiplier and again revealed that the photomultiplier is sensitive to light beyond its supposed measuring range at wavelength 302.8 nm. No VUV radiation at this wavelength was detected.

Several factors could play a role they include the factors mentioned in the previous section as well as the “beam overlap” and the magnitude of the resonant enhancement. The beam overlap of 2ω and ω is not ideal since the high intensity core of the ω beam is attenuated by the second harmonic generation process. The magnitude of the resonant enhancement is decreased due to the third photon’s wavelength being so far from the wavelength of the two-photon resonance. The largest short coming is believed to be the intensity of the light at wavelength 302.8 nm. The frequency doubling procedure produced a maximum of 0.13 mJ. An attempt to increase this by tighter focussing resulted in damage to the BBO crystal. In experiments by Jamroz *et al* [14] peak powers at this wavelength in the order of 5 - 25 kW led to resonant enhancement using the $4s6s\ ^1S$ level and sum frequency generation from 106.3 - 121 nm. Peak powers in this experiment were in the order of 4 kW. Phase matching could also play a role. No phase matching data was reported by Jamroz *et al* [14] or Herman *et al* [4]. The experiments were conducted at a fixed He pressure of 90 Torr as reported by Herman *et al* [4].

$^{12}\text{C}^{16}\text{O}$	Present Value (cm^{-1})	Literature Value (cm^{-1})	% Difference
$X^1\Sigma^+$	1.924	1.922	0.1
$A^1\Pi$	1.539	1.533	0.38

Table 4.2: Values of the rotational constant calculated for the lower state and the upper state. The calculated values compare favorably with those from literature [23].

4.4 Spectroscopy of CO with an Existing VUV source

4.4.1 Calibration and Results on Rotational Constants

The existing VUV setup discussed in section 3.2.5 was used to measure several rovibronic transitions of carbon monoxide. Rovibronic lines of $^{12}\text{C}^{16}\text{O}$ and $^{13}\text{C}^{16}\text{O}$ for the transition from the $X^1\Sigma^+$ ground state to the $A^1\Pi$ state in the (3-0) band were recorded and are shown in figure 4.14 and 4.15. The spectra were calibrated by comparing them with well known literature values [26] and then applying a linear least squares fit as illustrated in figure 4.16. A total of 30 lines were used in the calibration. R(0)-R(6), Q(1)-Q(6), P(2)-P(6) from $^{12}\text{C}^{16}\text{O}$ and R(0)-R(6), Q(1)-Q(4), P(2) from $^{13}\text{C}^{16}\text{O}$ were used. The accuracy of the calibration is 1×10^{-4} nm. The method of wave number differences as described in section 2.7 (equations 2.93, 2.94, 2.95, 2.96) was used to extract the rotational constants of $^{12}\text{C}^{16}\text{O}$ from the measured spectra of the $X^1\Sigma^+ - A^1\Pi$ (3 0) band. The wave number differences given by equations 2.93 and 2.94 were plotted versus the rotational quantum number J for $J = 1 - 5$. Linear fits of the form of equation 2.95 and 2.96 were made. The gradient of the linear fit is equal to $4B_v$. This is illustrated in figure 4.17. From the gradient of the graph it is possible to extract the rotational constants. The rotational constants measured compare well with those in the literature as illustrated in table 4.2 thus proving the accuracy of the calibration technique as well as the sensitivity of the LIF technique.

4.4.2 Optimisation of the Setup for the Detection of Forbidden Transitions

Several rovibronic transitions in the so called ‘‘forbidden bands’’ of $^{12}\text{C}^{16}\text{O}$ that have not been published before were measured and identified . These transitions

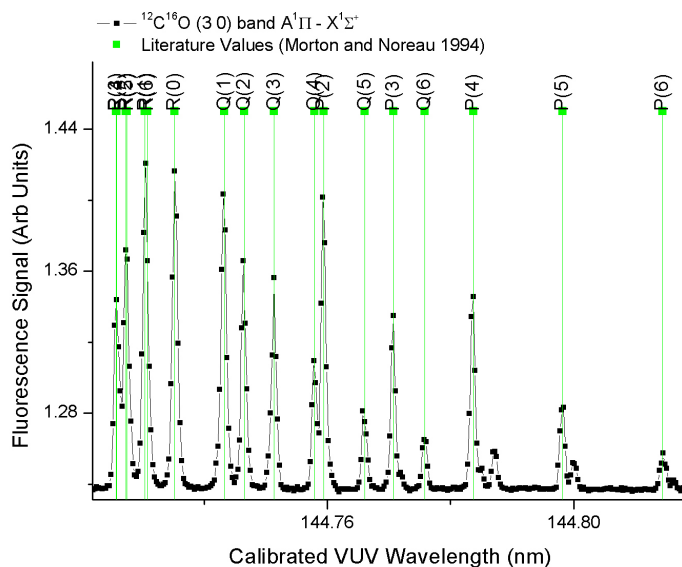


Figure 4.14: Calibrated spectrum of $^{12}\text{C}^{16}\text{O}$ from the $A^1\Pi - X^1\Sigma^+$ transition in the (3-0) band.

are from the singlet ground state of CO to one of the excited triplet states. The signals from these transitions are weak but due to the background free detection of signals in the LIF setup the signal to noise ratio is still large enough to be detected. There are three triplet states lying close to the well known A state, the $d^3\Lambda$, $e^3\Sigma^+$ and the $a^3\Sigma'$ state. The singlet-triplet rovibronic transitions that were investigated lie among several singlet-singlet $X^1\Sigma^+ - A^1\Pi$ (3 0) transitions. The singlet-singlet transitions normally dominate the spectra. It is possible to suppress the detection of the singlet-singlet transitions by making use of the longer fluorescence lifetime of the singlet-triplet transitions. This is done by measuring the fluorescence at a delayed time making use of the boxcar integrator. The boxcar integrator integrates the signal from the photomultiplier and then passes the integrated signal onto the computer for analysis. It is possible to set when this integration time begins (known as the gate delay) and over how much of the signal to integrate (known as the gate width). By delaying the integration time by a few hundred nanoseconds the fluorescence detected is almost exclusively from the singlet-triplet transitions. One of the recorded spectra is shown in figure 4.19. In this spectrum the gate delay was set to 350 ns and

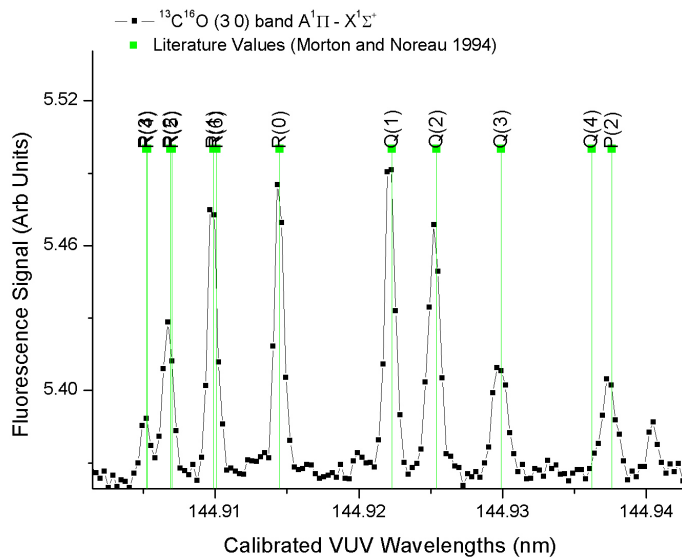


Figure 4.15: Calibrated spectrum of $^{13}\text{C}^{16}\text{O}$ from the $A^1\Pi - X^1\Sigma^+$ transition in the (3-0) band.

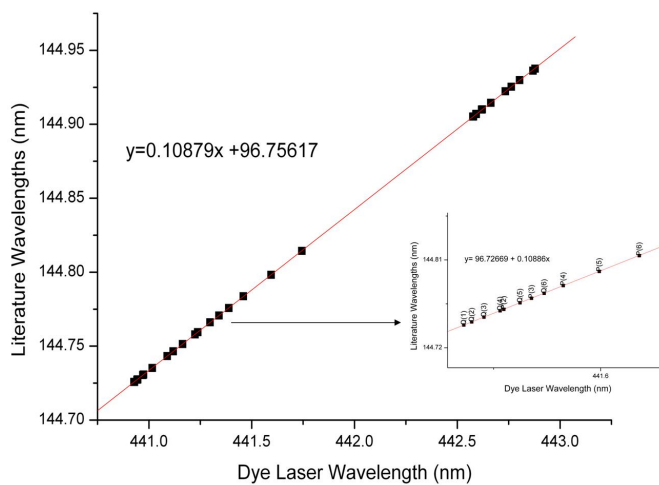


Figure 4.16: The calibration curve for the measurements of the singlet spectra of $^{12}\text{C}^{16}\text{O}$ and $^{13}\text{C}^{16}\text{O}$.

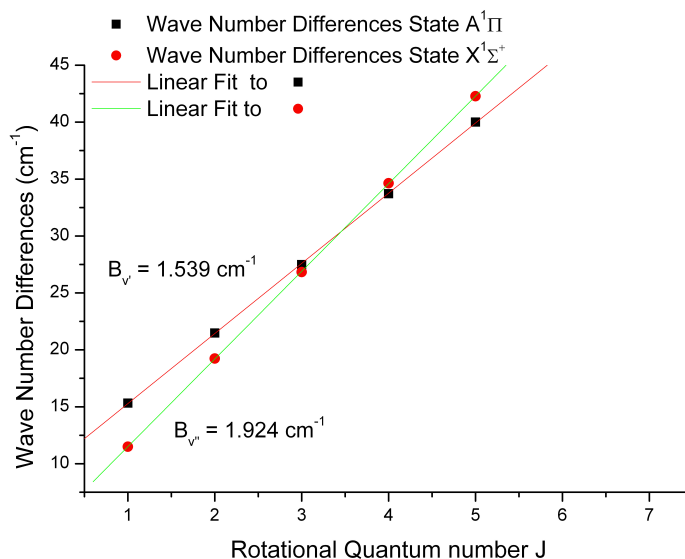


Figure 4.17: The rotational constants calculated from the spectra in figure 4.14.

the gate width was set to 180 ns with a delay between the laser pulse and the gas pulse of 500 μs . Figure 4.18 shows the signals of a single-singlet transition and a singlet-triplet transition. The gate width and gate delay optimised for the detection of the singlet-triplet transition. As can be seen in the figure for a pulse delay of 500 μs the signal of the singlet-singlet transition and the singlet-triplet transition are of the same order of magnitude. This is another method to suppress the detection of the singlet-singlet transitions in the recorded spectra. Due to the small signals of the singlet-triplet transitions it was found that the supply voltage to the Hamamatsu photomultiplier was optimal when set to its maximum of 2 kV. The signal to noise ratio of the singlet-triplet transitions was improved by using pure CO in the supersonic jet. The addition of argon as a collisional partner for CO resulted in a decrease in the signal to noise ratio. A pressure of 1 bar was used.

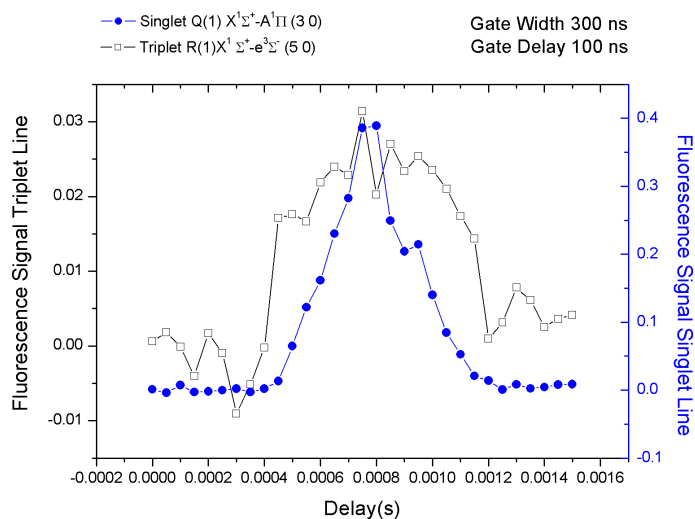


Figure 4.18: A comparison between the delay scans for a singlet-singlet transition and a singlet-triplet transition.

4.4.3 Results on Forbidden Transitions

A total of 20 new rovibronic transitions were identified shown in figure 4.19. The lines recorded in the spectra are from the (5 0) band of the $e^3\Sigma^- - X^1\Sigma^+$ transition. Five of these transitions could be resolved individually and calibrated wavelengths were obtained for these and are listed in table 4.3. These are indicated in figure 4.20 It was not possible to resolve the other 15 lines individually and so average wavelengths for these transitions were obtained as listed in table 4.4. These lines are shown in figure 4.21. The peaks labeled from A to E each consist of several closely spaced triplet transitions. The transitions that these peaks consist of are indicated in table 4.4. An average wavelength for each peak was assigned to all the lines that it consisted of.

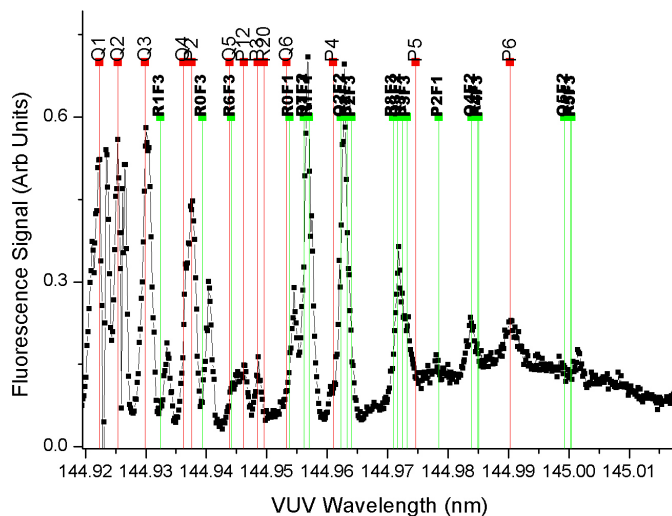


Figure 4.19: Spectrum of the identified triplet transitions of the $e^3\Sigma^- - X^1\Sigma^+$ (5 0) band of $^{12}\text{C}^{16}\text{O}$. The red lines represent the singlet transitions used for the calibration of the spectra.

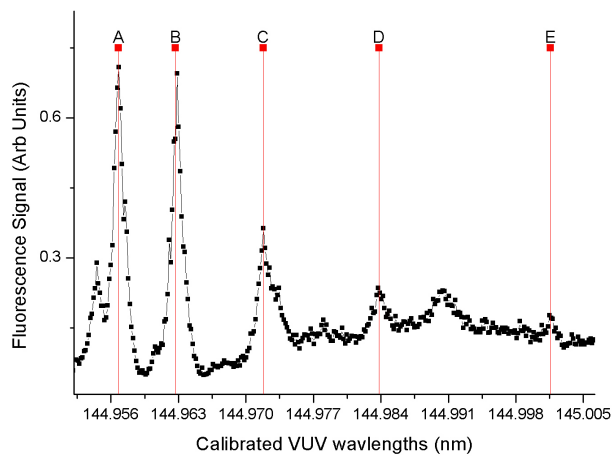


Figure 4.21: The triplet lines that could not be resolved. Each peak labelled in the figure consists of several closely spaced singlet-triplet transitions.

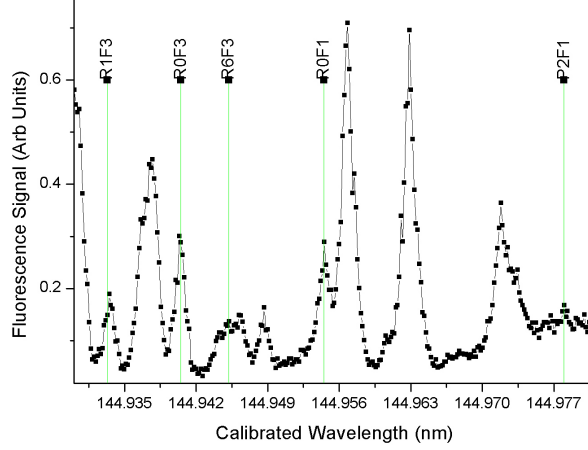


Figure 4.20: The five triplet lines that could be resolved.

Line	Calculated Wavelength (nm) [5]	Measured Wavelength (nm)	Wavelength Uncertainty ¹ (nm)	Difference between Calculated and Measured Wavelengths (nm)	Number of times observed
R0F1	144.9538	144.9552	4.61×10^{-4}	1.36×10^{-3}	15
R0F3	144.9394	144.9405	2.33×10^{-4}	1.0×10^{-3}	16
R1F3	144.9324	144.9333	1.91×10^{-4}	9.0×10^{-4}	16
R6F3	144.9441	144.9452	2.50×10^{-4}	1.0×10^{-3}	8
P2F1	144.9785	144.9793	1.2×10^{-3}	8.3×10^{-4}	3
Average ²			2×10^{-4}		

Table 4.3: Resolved triplet lines of the $e^3\Sigma^- - X^1\Sigma^+$ (5 0) band.

¹The standard deviation of the average wavelength for each transition is taken as the wavelength error.

²Standard deviation of the first four lines were used to calculate the average error.

Line	Peak Label	Calculated Wavelength (nm) [5]	Measured Wavelength (nm)	Difference between Calculated and Measured Wavelengths (nm)	Number of times observed
R1F1	A	144.957	144.9574	0.0004	15
Q1F2	A	144.9562	144.9574	0.0012	15
R7F3	A	144.9562	144.9574	0.0012	15
Q2F2	B	144.9623	144.9637	0.0014	15
P2F3	B	144.9641	144.9637	-0.0003	15
R2F1	B	144.9633	144.9637	0.0004	15
R3F1	C	144.9725	144.9734	0.0008	13
P3F3	C	144.9732	144.9734	0.0001	13
Q3F2	C	144.9716	144.9734	0.0017	13
R8F3	C	144.9709	144.9734	0.0024	13
Q4F2	D	144.9839	144.9838	-0.0001	1
R4F1	D	144.9849	144.9838	-0.0011	1
P4F3	D	144.9851	144.9838	-0.0013	1
R5F1	E	145.0003	145.0016	0.0013	1
P5F3	E	144.0005	145.0016	0.0011	1

Table 4.4: A table of measured transitions of the $e^3\Sigma^- - X^1\Sigma^+$ (5 0) band that could not be resolved individually.

For the five lines that could be resolved, their values were subtracted from the values calculated by Eidelsberg *et al* [5] as is indicated in figure 4.22. There is quite a substantial deviation from the zero line, this deviation can be attributed to one of two things: the measurements were not calibrated accurately or the literature values deviate from the true wavelengths of the transitions. A total of seven singlet lines of $^{13}\text{C}^{16}\text{O}$ were used in the calibration (Q(1)-Q(3), P(2), P(3), P(6) and P(12)) and the accuracy of the calibration is 1×10^{-4} nm. To test whether the literature values deviate from the true wavelengths of the transitions the average wavelength value for each line was taken and then subtracted from the literature wavelengths. This is plotted with the standard deviation of the measured wavelengths as error bars in figure 4.23. With the exception of the P2F1 line, which was rather weak and only detected in three of the recorded spectra, it is clear that the error in the measurement is less than the deviation from the zero line. An average deviation from the zero line was taken for the five transitions, this value was then subtracted from the initial measurements as is

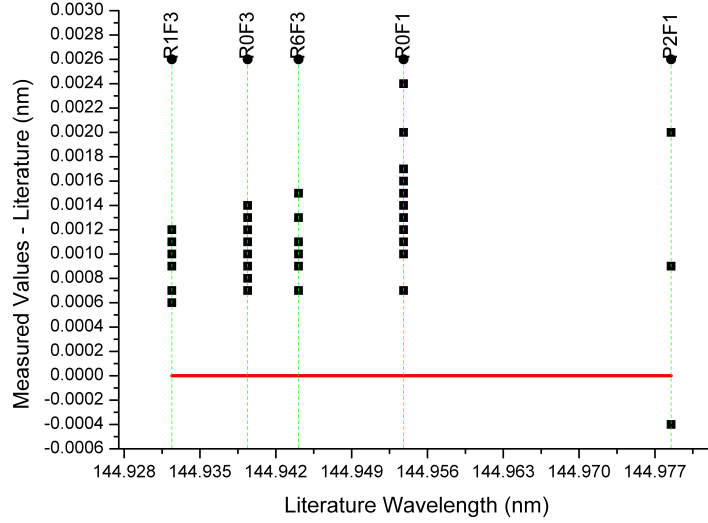


Figure 4.22: The measured values were subtracted from the literature values to see by how much they deviate.

shown in figure 4.24. The measured values are now spread around the zero line. The calculated literature values deviate from the measured values by 0.001(05) nm. We therefore conclude that the wavelengths calculated by Eidelsberg *et al* [5] deviate from the true transition wavelengths by 0.001(05) nm \pm 0.0002 nm.

This deviation was subtracted from the lines that we were not able to resolve. This provides insight into the transition that makes the greatest contribution to the peak. This is illustrated in figure 4.25. The average value is indicated by the open blue square. It can be argued that, if one of the lines contributing to the unresolved line is dominant, the peak of the unresolved line will lie close to the wavelength of that dominant line, therefore the measurements of the lines that are spaced closely around zero are thought to be the major contributor to the peak. The first peak, labeled peak A in figure 4.21 consists of the transitions Q1F2, R7F3 and R1F1. Q1F2 and R7F3 have the same calculated wavelength. R7F3 probably makes a small contribution due to the high rotational quantum number J equal to 7. From figure 4.25 it appears that both the R1F1 line and the Q1F2 line make an even contribution to the peak. The second peak, labeled peak B in figure 4.21 consists of the transitions

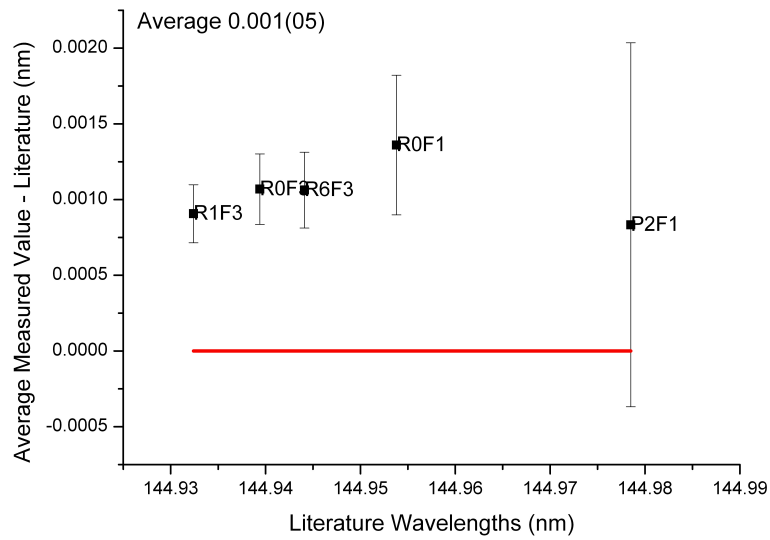


Figure 4.23: The average measurement for each transition was subtracted from the literature wavelengths.

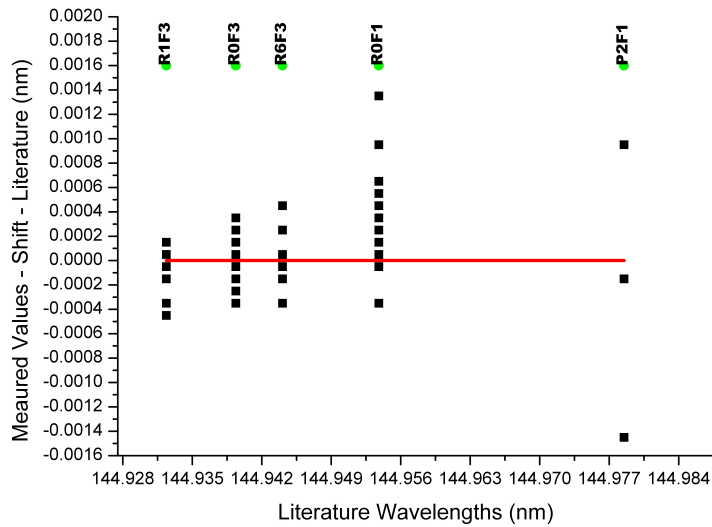


Figure 4.24: The measured values minus the average shift from the calculated literature values.

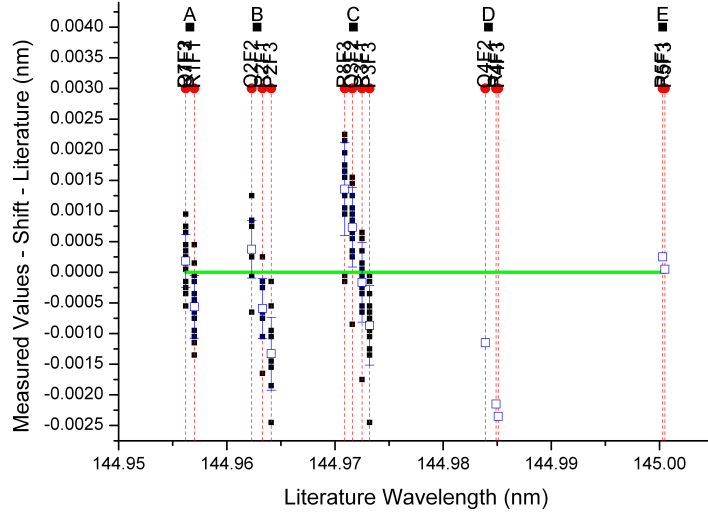


Figure 4.25: The lines that could not be resolved and their deviation from the calculated values in the literature.

Q2F2, R2F1 and P2F3. It is clear from figure 4.25 that The R2F1 line and the Q2F2 line contribute the most to the peak. The third peak, labeled peak C in figure 4.21, consists of four lines: R8F3, Q3F2, R3F1 and P3F3. It appears that the strongest contributor is the R3F1 line. The R8F3 line is expected to make a very small contribution to the intensity of the line due to the high J number equal to 8. The peaks labeled D and E in figure 4.21 consisted of the lines Q4F2, R4F1, P4F3 and R5F1, P5F1 respectively. They were only detected in one of the recorded spectra and therefore an average value could not be assigned to the peaks. It is suspected that the R and Q lines in these two peaks contribute the most if the trend from peaks A, B and C continue.

In summary we have obtained experimentally measured wavelengths for the first time for five lines in the $e^3\Sigma^- - X^1\Sigma^+(5\ 0)$ transition. A reduction in the VUV bandwidth will be necessary in order to resolve the remaining fifteen lines that were observed.

Chapter 5

Conclusion

5.1 Generation of VUV by Four-Wave-Mixing in Metal Vapours

It has been demonstrated that metal vapours can be used as nonlinear media for the generation of tuneable, coherent, narrow bandwidth radiation in the VUV region of the electromagnetic spectrum. The crossed heat pipe oven facilitates the generation of a stable homogeneous column of metal vapour and its applications in spectroscopy are well known. The crossed heat pipe ovens constructed and used in this study confirm this. The conditions in the existing Mg Kr heat pipe were optimised and the Mg medium used to generate tuneable VUV radiation by four wave sum frequency mixing. The generated VUV has sufficient power to detect weak lines of $^{13}\text{C}^{16}\text{O}$ and so called “forbidden transitions” of $^{12}\text{C}^{16}\text{O}$. The bandwidth of the VUV radiation is in the order of 0.0002 nm which is adequate to resolve rotational fine structure of CO spectra. In the newly constructed Zn heat pipe oven third harmonic generation was achieved using the $5s\ ^1S_0$ level but could not be reproduced consistently. The optimal operating characteristics are not known as yet and thus the signals that one is searching for are quite small. Measuring on a non-zero background due to a signal from the incident light limits the sensitivity of the detection. The detection system is thus one of the major limiting factors in this experiment. The incident power is another critical factor. It is believed that the incident laser intensity is simply not enough for such an unoptimised system.

Resonant enhancement using the $4s6s\ ^1S$ level and the subsequent generation

of sum frequency radiation at 121.12 nm was not achieved. Again the detection system is a limitation but the main reason it is believed that the experiment did not succeed is due to the intensity of the two-photon resonant light used to drive the nonlinear process. Second harmonic generation in the BBO crystal did not provide the necessary input intensity. It is also possible that phase matching and the focus of the beam played a role in the failure to generate sufficient VUV to detect sum frequency radiation at 121.12 nm.

5.2 VUV Spectroscopy of CO

One of the applications of such a source is the investigation of the rovibronic energy levels of Carbon Monoxide. In principle this can be extended to the investigation of any gas. The measured singlet-triplet transitions show how sensitive the LIF technique is and confirm that the tuneable VUV source is well suited for laser spectroscopy. In summary five never before measured singlet-triplet transitions of the $e^3\Sigma^- - X^1\Sigma^+(5\ 0)$ band of $^{12}\text{C}^{16}\text{O}$ for which no experimental measured wavelengths exist were observed and calibrated wavelengths assigned to them. Fifteen other singlet-triplet transitions were observed but could not be resolved completely. Instead the data provides an indication as to which transition contributes most strongly to the observed peak.

5.3 Proposed Future Work

The measurements taken with the existing setup can be continued to other rovibronic bands of CO. There are a host of intersystem transitions of CO that have not been verified experimentally [5]. Many of these transitions can be measured using the magnesium heat pipe oven and the LIF technique. The introduction of an interactivity etalon to the resonant dye laser would narrow the bandwidth of the generated VUV radiation. This could possibly aid in resolving some of the rovibronic transitions observed in the present study.

With regards to the zinc heat pipe, further optimisation of the setup for third harmonic generation needs to be done before the potential of the device as a spectroscopic instrument can be fully realised. There are a number of problems most notably the photomultiplier used in the detection of the VUV radiation. Once this problem is resolved possibly by separating the incident and

VUV beams the extension to sum frequency generation as outlined in section 3.2.5 should be achievable. The zinc heat pipe could then be used to continue the VUV spectroscopy wavelengths between 120 and 140 nm. The zinc heat pipe will lend itself to defect generation in large bandgap materials such as diamond and LiF. The VUV radiation can be used to generate defects in these materials and then the defects can be analysed through surface second harmonic generation. A better understanding of these defects could lead to the ability to produce a better quality synthetic diamond.

Bibliography

- [1] Y.R. Shen. *The Principles of Nonlinear Optics*. John Wiley and Sons Inc, 1984.
- [2] P.A. Franken A.E. Hill C.W. Peters and G. Weinreich. Generation of optical harmonics. *Phys. Rev. Lett.*, 7:118–119, 1961.
- [3] J.A. Armstrong N. Bloembergen J. Ducuing and P.S. Pershan. Interactions between light waves in a nonlinear dielectric. *Phys. Rev.*, 127(6):1918 – 1939, February 1962.
- [4] P. R. Herman P. E. LaRocque R. H. Lipson W. Jamroz and B. P. Stoicheff. Vacuum ultraviolet laser spectroscopy. iii: Laboratory sources of coherent radiation tunable from 105 to 175 nm using *Mg*, *Zn*, and *Hg* vapors. *Can. J. Phys.*, 63(12):1581–1588, 1985.
- [5] M. Eidelsberg and F. Rostas. An atlas of the intersystem transitions of *CO*. *Astrophys. J. Suppl. Ser.*, 145:89–109, 2002.
- [6] R.W. Boyd. *Nonlinear Optics*. Elsevier, 2003.
- [7] Wu Feng Tie and Zhang Wen Zhen. Consideration of angular acceptance angle in *BBO* crystal on a highly efficient second harmonic generation. *Optics and Laser Technology*, 30(3-4):189–192, 1998.
- [8] R.S. Adhav S.R. Adhav and J.M. Pelaprat. *BBO*'s nonlinear optical phase-matching properties. Technical report, Laser Focus, 1987.
- [9] M.J. Buerger. *Elementary Crystallography*. John Wiley and Sons, Inc, 1963.
- [10] J.E. Midwinter and J. Warner. The effects of phase matching method and of uniaxial crystal symmetry on the polar distribution of second-order nonlinear optical polarization. *Br. J. App. Phys.*, 16:1135–1142, August 1965.
- [11] M. Born and E. Wolf. *The Principles of Optics*. Pergamon Press, 1965.
- [12] J.D. Hey. Non-linear optics reviewed. part 1. *S. Afr. J. Phys.*, 5:6–18, 1982.

- [13] C. R. Vidal. *Topics in Applied Physics (Chapter 3)*. Springer-Verlag Berlin Heidelberg, 1987.
- [14] W. Jamroz P.E. LaRocque and B.P. Stoicheff. Generation of continuously tunable coherent vacuum-ultraviolet radiation [140 to 106 nm] in zinc vapour. *Opt. Lett.*, 7(12):617–619, 1982.
- [15] K. Yamanouchi and S. Tsuchiya. Tunable vacuum ultraviolet laser spectroscopy: excited state dynamics of jet-cooled molecules and van der waals complexes. *J. Phys. B*, 28:133–165, 1995.
- [16] H. Junginger H.B. Puell H. Scheingraber and C.R. Vidal. Resonant third harmonic generation in a low-loss medium. *IEEE J. Quantum Electron*, 10:1132, 1980.
- [17] T.J. McKee B.P. Stoicheff and Stephen C. Wallace. Tunable, coherent radiation in the lyman - alpha region (1210 - 1290 Å) using magnesium vapor. *Opt. Lett.*, 3:207–208, 1978.
- [18] R. Hilbig and R. Wallenstein. Resonant sum and difference frequency mixing in Hg. *IEEE J. Quantum Electronics*, QE-19:1759–1770, 1983.
- [19] P.E. LaRocque W. Jamroz and B.P. Stoicheff. Resonantly enhanced second-harmonic generation in zinc vapor. *Opt. Lett.*, 7(4):148–150, 1982.
- [20] G.M. Grover T.P. Cotter and G.F. Erickson. Structures of very high thermal conductance. *J. App. Phys.*, 35:1990, 1963.
- [21] K. Cornwell. *The Flow of Heat*. Van Nostrand Reinhold Company, 1977.
- [22] C.R. Vidal and J. Cooper. Heat-pipe oven: A new, well defined metal vapour device for spectroscopic measurements. *J. App. Phys.*, 40:3370, 1969.
- [23] G.H. Herzberg. *Spectra of Diatomic Molecules*. D.Van Nostrand Company, 1950.
- [24] O.R. Gilliam C.M. Johnson and W. Gordy. Microwave spectroscopy in the region from two to three millimeters. *Phys. Rev.*, 78:140–148, 1950.
- [25] T.W. Swaddle. *Inorganic Chemistry*. Academic Press, 1997.
- [26] D.C. Morton and L. Noreau. A compilation of electronic transitions in the CO molecule and the interpretation of some puzzling interstellar absorption features. *Astrophys. J. Suppl. Ser.*, 95:301–343, 1994.
- [27] A. du Plessis E.G. Rohwer and C.M. Steenkamp. Accurate laboratory wavelengths of the $A^1\Pi(v' = 0 - 5)$ - $X^1\Sigma^+(v'' = 0)$ vibronic bands of $^{12}C^{17}O$ and $^{12}C^{18}O$. *Astrophys. J. Suppl. Ser.*, 165(1):432–437, 2006.

- [28] A. Mellinger. *Untersuchung hochangeregter Triplettzustände des CO-Moleküls*. PhD thesis, Technische Universität München angefertigt am Max-Planck-Institut für extraterrestrische Physik, 1995.
- [29] A. Du Plessis. *High Resolution Spectroscopy of CO*. PhD thesis, University of Stellenbosch, 2006.
- [30] K.H. Strobl and C.R. Vidal. Radiative lifetimes of selected rovibronic triplet levels of the *CO* molecule. *J. Chem. Phys.*, 86:62–70, 1987.
- [31] H. Haken and H.C. Wolf. *Molecular physics and elements of quantum chemistry*. Springer-Verlag, Berlin, 1994.
- [32] S. H. Ashworth and J. M. Brown. *An Atlas of Optogalvanic Transitions in Neon*. Rutherford Appleton Laboratory, 1991.
- [33] C.M. Steinmann. Development and characterisation of a tunable laser source in the vacuum ultraviolet. Master's thesis, University of Stellenbosch, 2000.
- [34] Lambda Physik, Hans-Brockler-Street 12, D-3400 Göttingen Germany. *Dye Laser FL 3001/3002 Preliminary Instruction Manual*, first edition edition, May 1986.
- [35] www.redoptronics.com. Manufacturers of *BBO* crystals. Technical report, 2008.